




University of  
Stavanger

**Faculty of Science and Technology**

## **MASTER'S THESIS**

|  |  |
|--|--|
| Study program/Specialization:<br>Engineering Structures and Materials/<br>Civil and Offshore structures.                 | Spring semester, 2022<br><br>Open / Restricted access  |
| Writer:<br>Nour Tayem  | <br>(Writer's signature) |
| Faculty supervisor: Dimitrios G. Pavlou<br><br>External supervisor(s): Dimitrios G. Pavlou                               |  |
| Thesis title:<br><br>Life Prediction for metals under multiaxial fatigue: A Review of existing multiaxial fatigue tests. |  |
| Credits (ECTS): 30   |  |
| Key words:<br><br>Multiaxial<br><br>Uniaxial<br><br>Fatigue test   | Pages: 67<br><br>+ enclosure: 0<br><br>Stavanger, 15.06.2022<br>Date/year                                  |

## **Acknowledgment**

The Master's thesis was completed in the spring of 2022 as part of the University of Stavanger's two-year Master's Degree Programme in Engineering Structures and Materials.

I hope that anyone who reads it will find it entertaining and inspiring, and that the effort will provide information and suggestions for future efforts and industry expansion.

I would also like to thank my supervisor, Prof. Dimitrios G. Pavlou. He has always offered valuable feedbacks and suggestions that have helped to enhance this study.

I am really appreciative of my family's ongoing encouragement and unwavering support. Without their love and support, this adventure wouldn't have been possible. In addition, without their advice, I would never have attained the significant milestones in my life and career.

## **Abstract**

An overview of multiaxial fatigue life prediction methodologies and tests is provided in the present paper. It is essential for engineering applications to accurately estimate the fatigue failure behaviour and fatigue life of structures or materials subjected to multiaxial loads. Several multiaxial fatigue criteria and metal materials are reviewed in this research, including materials such as steel S355, titanium alloy TC4, 42CrMo4, AISI 303, SM45C, SAE1045, and LY12CZ.

It is noted that if the fatigue life prediction models created under multiaxial constant amplitude loading were applied to the life prediction of the complicated multiaxial load, right techniques for the critical plane determination and multiaxial fatigue damage parameter setting would be required.

Multiaxial stress experiments are much more complicated and costly than uniaxial fatigue experiments. Unfortunately, neither the damage produced by a multiaxial fatigue stress state nor the method for assessing it are well recognized.

Consequently, it is a fully unexplored subject that continues to be investigated. Existing multiaxial non-proportional fatigue methods are restricted to the theoretical research phase, with limited practical applications. The fundamental reason is that the engineering load is complicated and unpredictable. As mentioned, multiaxial fatigue is a complicated phenomenon; thus, it should not be transformed into an equal condition of uniaxial stress using a simple static premise.

# Contents

|   |      |
|---|------|
| Acknowledgment .....  | i    |
| List of Figures .....   | v    |
| List of Tables .....  | vii  |
| List of Notations .....   | viii |
| 1. Introduction .....   | 1    |
| 1.1 Failures and accidents due to multiaxial fatigue.....                 | 2    |
| 1.2 The Development of a Multiaxial Fatigue Experiment.....               | 3    |
| 1.3 Objective .....   | 4    |
| 2 Theory.....   | 5    |
| 2.3 A Review on Fatigue: .....  | 5    |
| 2.2.1 Definition:.....  | 5    |
| 2.2.2 Mechanisms of metal fatigue.....                                    | 7    |
| 2.2.3 Mechanisms of destruction .....                                     | 7    |
| 2.2.4 Fatigue stages, contributory factors, and treatment regimens: ..... | 8    |
| 2.3 Multiaxial Fatigue Models .....                                       | 11   |
| 2.4 A Review of existing multiaxial fatigue tests .....                   | 12   |
| 3 Method.....   | 24   |
| 3.1 Conventional Methods: .....   | 24   |
| 3.1.1 S-N Curves .....  | 24   |
| 3.1.2 Fatigue curve: .....  | 25   |
| 3.2 Multiaxial Fatigue Models .....                                       | 29   |
| 3.2.1 Stress Based Multiaxial Fatigue Models .....                        | 29   |
| 3.2.2 Models Based on Empirical Formulas.....                             | 29   |
| 3.2.3 Gough and Pollard Model.....  | 29   |

|   |    |
|---|----|
| 3.2.4 Models of Equivalent Stress .....   | 29 |
| 3.2.5 Maximum Principal Stress Model .....  | 29 |
| 3.2.6 Maximum Shear Stress (Tresca) The Tresca criteria can also be applied to fatigue,<br>with the assumption that the starting crack occurs when the following conditions are met.<br>..... | 30 |
| 3.2.7 Von Mises Model .....   | 30 |
| 3.2.8 Sines Model .....   | 30 |
| 3.2.9 Crossland Model.....  | 32 |
| 3.3 Models of critical planes. ....   | 32 |
| 3.3.1 The Fatemi and Socie critical plane model .....   | 32 |
| 3.3.2 McDiarmid Model .....   | 33 |
| 3.3.4 Dang Van Model .....  | 34 |
| 3.3.5 Brown and Miller Model .....  | 34 |
| 3.3.6 Smith–Watson–Topper Model .....   | 35 |
| 3.3.7 Liu’s Virtual Strain Energy Model.....  | 35 |
| 4 Results and Discussion .....  | 36 |
| 5 Conclusion and Recommendation .....   | 63 |
| 6 Reference .....   | 65 |

## List of Figures

|  |    |
|--|----|
| Figure 2.1 Cycle loading.....  | 5  |
| Figure 2.2 Different stress ratios.....  | 6  |
| Figure 2.3 Fatigue stages. ....  | 8  |
| Figure 2.4 Fatigue-related life domains.....   | 10 |
| Figure 2.5 Proportional and non-proportional loading. ....   | 11 |
| Figure 2.6 Hourglass specimen.....   | 14 |
| Figure 2.7 Microstructure of S355 steel. ....  | 15 |
| Figure 2.8 Specimen geometry for biaxial cyclic tension–compression with cyclic<br>torsion tests. ....                             | 18 |
| Figure 2.9 Microstructure typical of titanium alloy TC4.....   | 19 |
| Figure 2.10 Specimen geometry. ....  | 19 |
| Figure 3.1 S-N curve.....  | 25 |
| Figure 3.2 Fatigue diagram as a cross plot of S-N curves. ....   | 26 |
| Figure 3.3 Gerber fatigue limit .....  | 27 |
| Figure 3.4 Goodman fatigue diagram .....   | 28 |
| Figure 3.5 Soderberg fatigue diagram .....   | 28 |
| Figure 4.1 Specimens after axial fatigue tests. ....   | 38 |
| Figure 4.2 Specimens after multiaxial fatigue tests.....   | 38 |
| Figure 4.3 Specimen tested under $\sigma_a = 207$ MPa with $R = 0.01$ . ....   | 38 |
| Figure 4.4 Specimen tested under $\sigma_a = 272$ MPa with $R = -1$ .....  | 39 |
| Figure 4.5 Specimen tested under $\sigma_a = 168$ MPa and $\tau_a = 84$ MPa with $R = 0.01$ .....                                  | 39 |
| Figure 4.6 Specimen tested under $\sigma_a = 204$ MPa and $\tau_a = 104$ MPa with $R = -1$ .....                                   | 39 |
| Figure 4.7 Multi-axial fatigue loading paths.....  | 40 |
| Figure 4.8 Fractographic analyses of the fatigue failure plane orientations under each<br>of the six loading paths (42CrMo4).....  | 41 |
| Figure 4.9 Fractographic analyses of the fatigue failure plane orientations under each<br>of the six loading paths (AISI 303)..... | 42 |
| Figure 4.10 Uniaxial fatigue data.....   | 49 |
| Figure 4.11 Nonproportional strain paths. ....   | 51 |
| Figure 4.12 Prediction of the service life of SM45C.....   | 54 |

|   |    |
|---|----|
| Figure 4.13 Prediction of the service life of SAE1045 .....   | 56 |
| Figure 4.14 SAE1045 life prediction. ....   | 59 |
| Figure 4.15 LY12CZ life prediction under uniaxial tension/compression and pure<br>torsion loads. .... | 62 |

## List of Tables

|  |    |
|--|----|
| Table 2.1 Mechanical properties.....   | 13 |
| Table 2.2 Chemical composition. ....   | 13 |
| Table 2.3 Monotonic and cyclic mechanical properties. ....                           | 17 |
| Table 2.4 Chemical compositions of the materials studied in (wt%). ....              | 17 |
| Table 2.5 The chemical composition of TC4 (wt%).....                                 | 19 |
| Table 2.6 Fatigue and cyclic stress–strain properties of titanium alloy TC4.....     | 20 |
| Table 2.7 Chemistry of the material Ti-6Al-4V. ....                                  | 21 |
| Table 2.8 Material Properties for Ti-6Al-4V.....                                     | 22 |
| Table 2.9 Mechanical parameters of various materials .....                           | 23 |
| Table 4.1 Result of uniaxial and multiaxial tests.....                               | 37 |
| Table 4.2 Comparison of the observed crack plane with predictions for 42CrMo4....    | 43 |
| Table 4.3 Comparison of the observed crack plane with predictions for AISI 303.....  | 44 |
| Table 4.4 Loading vs measured crack plane results for AISI 303, loading Case 2. .... | 45 |
| Table 4.5 The experimental results for titanium alloy TC4.....                       | 46 |
| Table 4.6 The experimental results for titanium alloy TC4.....                       | 47 |
| Table 4.7 The experimental results Ti-6Al-4V.....                                    | 50 |
| Table 4.8 Test data of SM45C .....   | 52 |
| Table 4.9 Test data of SAE 1045 tension-torsion loading .....                        | 54 |
| Table 4.10 Test data of SAE 1045 bending-torsion loading.....                        | 57 |
| Table 4.11 Test data of LY12CZ. ....   | 60 |



## List of Notations

|                        |   |
|------------------------|---|
| $R$                    | Stress ratio                              |
| $\sigma_a$             | Alternating normal stress                 |
| $\sigma_{\max}$        | Maximum normal stress                     |
| $\sigma_{\min}$        | Minimum normal stress                     |
| $N_f$                  | Number of cycles until failure            |
| $\sigma_E$             | Maximum principal stress damage parameter |
| $\tau_E$               | Tresca damage parameter                   |
| $\sigma_{h\max}$       | Maximum hydrostatic stress                |
| $\sigma_{V M,m}$       | Von Mises mean stress                     |
| $\sigma_{V M,a}$       | Von Mises stress amplitude                |
| $\alpha_{V M}$         | Mean stress intensity factor              |
| $\sigma_{\text{mean}}$ | Mean normal stress                        |
| $\sigma_{\theta\min}$  | Minimum normal stress on a $\theta$ plane |
| $\sigma'_f$            | Fatigue strength at one cycle             |
| $b$                    | Material constant of Basquin model        |
| $E$                    | Young Modulus                             |
| $G$                    | Shear modulus.                            |
| $f_y$                  | Yield Strength                            |
| $f_u$                  | Fracture Strength                         |
| $\sigma_x$             | Normal stress in the direction of x axis  |
| $\sigma_y$             | Normal stress in the direction of y axis  |
| $\sigma_{n,\max}$      | Maximum normal stress                     |
| $\sigma_{\text{ut}}$   | Ultimate strength                         |

|                       |  |
|-----------------------|--|
| $\sigma_{hmean}$      | Hydrostatic stress for mean stresses             |
| $\tau_f$              | Coefficient of shear fatigue strength.           |
| $\tau_{a,oct}$        | Amplitude of the octahedral shear stress         |
| $\tau_{max}$          | Maximum shear stress                             |
| $b\gamma$             | Exponent of shear fatigue strength.              |
| $\gamma_f$            | Ductility coefficient of shear fatigue strength. |
| $c\gamma$             | Exponent coefficient of shear fatigue strength.  |
| $\Delta\gamma$        | Shear strain range                               |
| $\Delta\tau$          | Shear stress range                               |
| $\Delta\varepsilon_n$ | Normal strain range                              |
| $\Delta\sigma_n$      | Normal stress range                              |
| $K'$                  | Strength coefficient                             |
| $\varepsilon'_f$      | Fatigue ductility coefficient                    |
| $C$                   | Fatigue ductility exponent                       |
| $n'$                  | Strain hardening exponent                        |

## 1. Introduction

The majority of mechanical failures are caused by fatigue. Despite this, tiredness processes remain incompletely understood. This is due in part to the complex loadings of engineering components, structures, and complicated geometrical forms, which result in multiaxial cyclic stress-strain states as opposed to uniaxial. Typical examples are gas turbines, pressure vessels, nuclear reactors, ground vehicles, airplanes, and crankshafts. Although several multiaxial fatigue life prediction techniques have been presented, there is still no widely accepted solution. Engineering has achieved several technical improvements during the last two centuries. For example, it is now feasible to fly quicker between Europe and Africa than it was a century ago. The advancements made in the transportation industry, which is a critical component of the global economy and trading, are critical because the economy is highly dependent on products and services, which means that the transportation industry must be efficient in order to deliver those products and services faster and cheaper. Thus, efficiency requires engineers to verify both the durability and functioning of each component.

Most critical components used in the transportation sector are constructed of metals that undergo periodic load variations while in operation. Over time, these changes in stress might result in component failure. When a component is produced, it is intended to fulfil a certain function for a specified period before being fixed or removed. However, many components fail before they reach the end of their planned life cycle, resulting in a variety of unpleasant outcomes such as harm to other components, the environment, loss of human life, financial losses, and the expense of repairing or even replacing the component.

Over time, new technologies have been developed, posing additional hurdles for those responsible for engineering design. The deployment of new technologies may require both more efficient material utilisation and material improvement. Fracture and deformation are seen as significant economic issues, particularly in the motor vehicle and aerospace industries. The financial cost of preventing fracture and the problems related to it is about 4% of the gross national product in different areas of the economy (Shetty, 2013).

Throughout the twentieth century, several accidents were caused by fatigue failure. For instance, in 1954, a British commercial aircraft, dubbed the de Havilland Comet, crashed at a high height, resulting in several fatalities, and leading the British to lose their dominance in the transportation business. The accident was caused by a rivet that was not properly punched into the aircraft during construction, resulting in a microscopic manufacturing defect. This defect was created because of pressurisation systems exerting enormous strain on the fuselage, causing stress to the skin, particularly around the window doors. Repeated pressure transformed the manufacturing flaw into a fatigue fracture that grew over time, eventually resulting in a catastrophic breakdown.

### **1.1 Failures and accidents due to multiaxial fatigue**

The fracture mechanics hypothesis is predicated on the idea that a break already exists in a material and will grow until it becomes critical. The purpose of this theory is to anticipate the applied load at which the fracture length propagation will be the quickest until it reaches a critical point. Engineers must be able to estimate or quantify pre-existing fractures and compute their relative stress intensity factor to relate to the material fracture toughness during the design stage. Knowing the origin of a material's first fracture enables engineers to track its behaviour before it reaches a critical point. Milne (1994) believes that using a fracture mechanics method is the best way to control structural integrity since this theory has been shown to be trustworthy in a variety of high-tech applications (Milne, 1994).

Numerous studies have been conducted in the past to determine the economic impact of fracture failure in industrialised economies. Most of the financial loss associated with fracture failure is due to a variety of factors (Milne et al., 2003):

- replacement costs, including direct repair: components being unavailable, or revenue lost while services are located.
- costs of locating replacement services or components to maintain business operations during unavailability.
- costs of consequential damage.
- consequential costs to avoid failure on similar items.
- total loss of business or public image.
- costs of otherwise unnecessary activities.

- and costs of safety-related issues, including insurance costs.

It is critical to understand why some components or structures fail before their anticipated lifespan. Because it enables design engineers to include failure analysis into the early phases of the design process by eliminating variables that enhance the likelihood of a component failing. Understanding the failure process also enables maintenance professionals to detect early warning indications of fatigue failure.

Numerous structures and equipment are often exposed to multiaxial, complicated stresses. However, in the early years, complicated multiaxial stress was equated to uniaxial stress using static strength theory, and subsequently, multiaxial fatigue issues were addressed using uniaxial fatigue theory. While this strategy is efficient for multiaxial proportional loads, it is ineffective for multiaxial non-proportional loads that are more comparable to real loads. In comparison to uniaxial fatigue, multiaxial fatigue is more complex in terms of experimental study, mechanics analysis, and physics mechanism, among other features. Thus, since the 1970s, researchers have focused on the study of multiaxial fatigue, which is more applicable to real-world loads, and it has been the field's focal point (Carpinteri et al., 2011; Jahed et al., 2007).

## **1.2 The Development of a Multiaxial Fatigue Experiment**

Now, there are primarily three types of multiaxial fatigue test machines: tension-torsion, bend-torsion, and biaxial tension-compression fatigue test machines (Wang et al., 2010). A typical multiaxial fatigue specimen consists of a solid notched circular specimen or a thin-walled tubular specimen that has been subjected to tension torsion or inside-outside stress loads, a cruciform specimen that has been subjected to cross tension loading, and a plate-type specimen or a circular specimen that has been subjected to bend-torsion loading. The later specimens' localised stress and strain are not as straightforward as the thin-walled tubular specimens. It must be computed using the finite element approach due to the difficulty of measuring strains that vary with thickness. These specimens are frequently used to investigate the crack initiation and propagation characteristics of multiaxial fatigue (Miller et al., 1985).

The thin-walled tubular specimen exposed to tension-torsion stresses is utilised to investigate multiaxial fatigue life prediction. Since there is little stress gradient

between the interior and outer surfaces of the thin-walled tube, stress and strain may be readily monitored. However, it suffers from the difficulties inherent in manufacturing and the high cost of testing.

### **1.3 Objective**

The objective of this thesis is to investigate whether multiaxial fatigue is more or less dangerous for metals and structures. This is accomplished by reviewing a compilation of current multiaxial fatigue tests.

## 2 Theory

### 2.3 A Review on Fatigue:

#### 2.2.1 Definition:

Fatigue is described as a failure produced by a repetitive load that is less than the stress level required to induce a static failure, and it might be mechanical, thermal, or other in nature (Kamal & Rahman, 2018). In search of a more traditional description, the process of progressive localized permanent structural change happening in a material subjected to conditions that cause fluctuating stresses and strains at some point or points, which may end in cracks or total fracture after a sufficient number of fluctuations. There are many characteristics and parameters that need to be mentioned in relation to this occurrence in order to define it. Fatigue life, which is represented by the number of cycles until material failure, is one of them. Another is the stress ratio  $R$ , which is derived as the algebraic relationship between two loading factors that relate to each cycle. Due to this final variable, other loading parameters must be defined, including the minimum stress  $\sigma_{\min}$ , the maximum stress  $\sigma_{\max}$ , the mean stress  $\sigma_{\text{mean}}$ , and the stress amplitude (a) (ASTM, 2013; Lee et al., 2011). These variables are shown in Figure 2.1 and are linked by Equations 2.1, 2.2, and 2.3.

$$R = \frac{\sigma_{\min}}{\sigma_{\max}} \quad (2.1)$$

$$\sigma_{\text{mean}} = \frac{\sigma_{\max} + \sigma_{\min}}{2} \quad (2.2)$$

$$\sigma_a = \frac{\sigma_{\max} - \sigma_{\min}}{2} \quad (2.3)$$

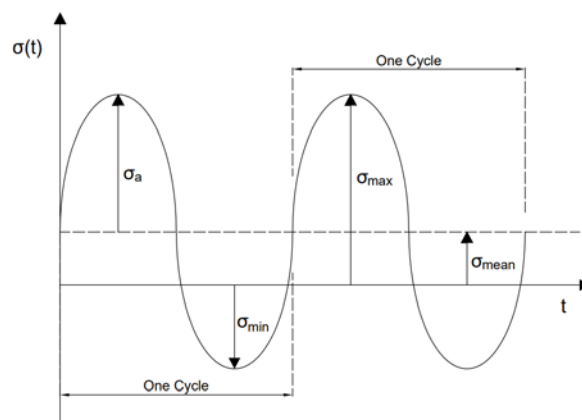


Figure 2.1 Cycle loading (Lee et al., 2011).

Thus, a stress-fatigue cycle may be characterized by three distinct pairs of parameters: minimum and maximum stress; mean and amplitude of stress; or amplitude of stress and ratio of stress. However, the loading wave shape must also be described in order to figure out the stress cycle for the metal. The loading spectrum is shown as a sinusoidal wave in Figures 2.1 and 2.2, although it may take on a variety of different and more complicated patterns. When it comes to time-dependent phenomena like creep or corrosion, the shape wave and frequency may have a significant impact on fatigue life (Schijve, 2003).

According to the mean stress value, the loading may be categorized as oscillating ( $R > 0$ ), entirely reversed ( $R = 1$ ), repeating ( $R = 0$ ), or reversed ( $R < 0$ ) (Lee et al., 2011).

The fatigue limit ( $\sigma_{fo}$ ) may be defined as the maximum cyclic loading that does not lead to a fatigue failure (Schijve, 2003).

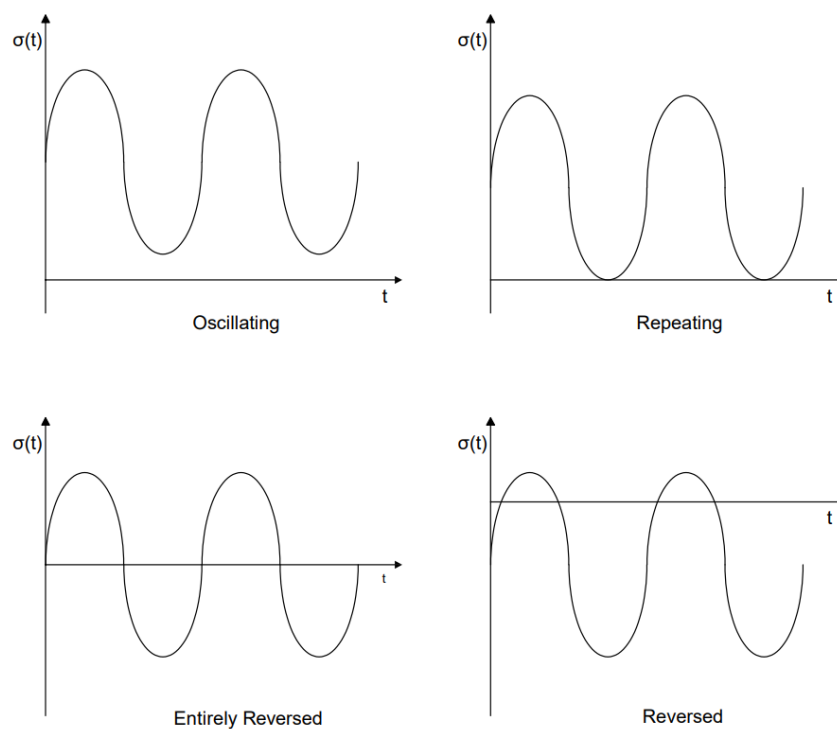


Figure 2.2 Different stress ratios (Schijve, 2003).



## **2.2.2 Mechanisms of metal fatigue**

Fatigue is a kind of failure that happens when cyclic stress is applied to a structural material over time. Over time, the cumulative damage from each cycle approaches a critical point, resulting in failure. Therefore, fatigue may occur in failures at loads much less than the maximum value, in contrast to most failure types. Fatigue is a three-stage process that includes the following (Sæstad, 2015):

### **2.2.2.1 Crack initiation:**

Cyclic loading may result in tiny surface discontinuities caused by dislocation slip steps. These discontinuities can also operate as stress raisers and, hence, as crack initiation sites. This applies only to components that are free of other material faults. In most situations, the fracture begins at a site of high stress due to material flaws. Scratches, dents, and flaws in welds are all examples of such faults.

### **2.2.2.2 Propagation of cracks:**

In contrast to the crack initiation stage, the crack propagation stage is more well known, and several theories exist to predict crack development, namely fracture mechanics. The primary factor affecting fracture propagation is the stress range experienced by the structural detail. Additionally, the initial fracture size has a significant effect on the structural detail's fatigue life.

### **2.2.2.3 Fracture final:**

When the crack size propagates to a critical size, the structural details will finally fracture. The ultimate fracture is determined by several characteristics, including the degree of stress, the size of the crack, and the hardness of the material. As with crack initiation, the fatigue life of the ultimate fracture is a tiny fraction of the total and is often insignificant in comparison to the crack propagation stage.

## **2.2.3 Mechanisms of destruction**

In general, fatigue life consists of fracture nucleation and propagation. Cracks often initiate in ductile-behaving materials along slip systems that are aligned with the greatest shear planes. Cracks often nucleate directly at discontinuities such as inclusions and voids in brittle materials, but they may also nucleate in shear. Once cracks develop, their growth may be classified into two stages: stage I, which corresponds to microcrack

growth (i.e., early growth) along maximum shear planes, and stage II, which corresponds to crack growth along maximum tensile stress planes. Microcrack growth is often dominated by stage I growth in ductile-behaving materials, while stage II development is typically dominated by stage I growth in brittle-behaving materials (Fatemi & Shamsaei, 2010).

#### 2.2.4 Fatigue stages, contributory factors, and treatment regimens:

The fatigue life cycle is classified into three distinct stages: initiation/nucleation, crack development, and final failure Figure. 2.3. These fatigue phases are influenced by a variety of factors; for example, the surface state impacts just the first stage, but corrosion influences both the fracture initiation and propagation stages, although to varying degrees. Consequently, the methods for estimating the fatigue life of initiation and fracture development should be different (Schijve, 2003).

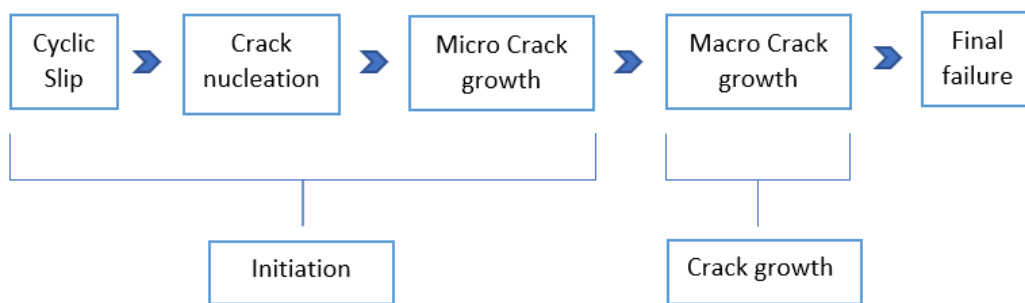


Figure 2.3 Fatigue stages (Dantas, 2019).

Nonetheless, most of the fatigue life takes place during the initial phase. The initiation is intended to have some microcracks that are not visible to the human eye until the failure stage. The fracture begins at the material's surface due to a variety of variables, such as surface roughness, corrosion pits, and less restriction on slip band movement. With regards to the last aspect, it is necessary to clarify that fatigue damage occurs as a result of slip band dislocations and the microcracks that develop along them. Following the initiation stage, the fracture usually moves away from the slip band direction and grows in the opposite direction to the loading direction (Schijve, 2003).

Apart from the surface state, other material factors influence the initiation phase and must be considered, including grain size and shape, anisotropy, lattice crystal type,

composition, crystal orientation change, composition, and the presence of inclusions (Schijve, 2003).

Relative to the fatigue life, residual stresses have a significant influence on it, with a positive effect in the case of compressive residual stresses and a mostly negative effect in the case of tensile residual stresses. In general, the ultimate tensile strength of a material is also a significant determinant in the fatigue behaviour of the material. Furthermore, when it comes to component characteristics, the geometry must be considered since it might result in a concentration of stresses, which necessitates the use of corrective factors such as the stress concentration factor  $K_f$  (Hudok, 1990).

There are two primary types of fatigue regimes: low cycle fatigue LCF and high cycle fatigue (HCF), each with its own set of features that must be considered. These two regimes are shown in Figure 2.4 by an S-N curve, which is a visual representation of the fatigue life of a component or material that will be discussed in subsequent sections. More and more research is being conducted on different fatigue regimens, such as extremely high cycle fatigue and very low cycle fatigue, which have been the focus of attention in recent years (Lee et al., 2011).

Low cycle fatigue regimes are characterized by short fatigue life and high loads that are typically less than  $10^4$  cycles. Since the first cycle, the material has been subjected to microplastic deformation in this regime. On the other hand, in the case of a high cycle fatigue regime, an elastic deformation state is present, and it is noticed that the life is increased between the  $10^4$  and  $10^7$  number of cycles. As a result, the fracture initiation process takes up a significant portion of the fatigue life under the high cycle regime.

The transition from one regime to another has not been well defined, and the fundamental distinction between them is based on the forms of deformation that have already been mentioned. As a result of these distinctions, the methodologies that are more appropriate and are used to assess the fatigue life are diverse and are based on various criteria for each regime of operation. For example, the strain technique is used by the majority of LCF models, but the stress approach is used by the majority of HCF models (Schijve, 2003; Socie, 1993).

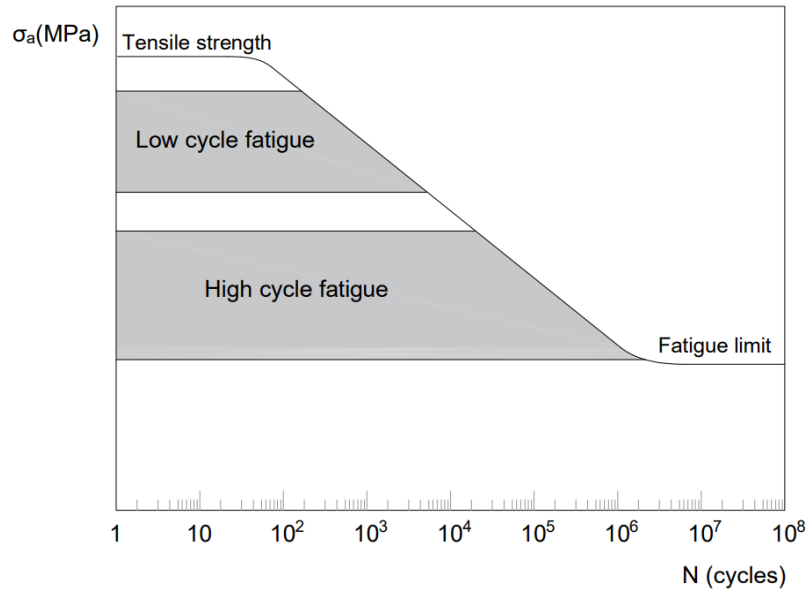


Figure 2.4 Fatigue-related life domains (Dantas, 2019).

The amplitude of the stress has a significant effect on fatigue damage, and the mean stress is a component that demands equal attention in the high cycle fatigue regime because it impacts the opening or shutting of microcracks. For instance, a compressive mean normal stress aids in the closure of microcracks, hence increasing fatigue resistance, but a tensile mean normal stress has the reverse effect. As a result, there are several models that account for the mean stress impact, as detailed in the following sections (Lee et al., 2011).

## 2.2 Multiaxial Fatigue State

Until recently, fatigue has been seen as a uniaxial condition, and all the methodologies discussed above have been developed for that stress state. However, reality is seldom uniaxial: it is often a complicated multiaxial stress condition. This fatigue condition affects a huge range of engineering structures, including wind turbine towers, bridges, and offshore structures. Regrettably, the extent of the damage produced by a multiaxial fatigue stress condition, as well as the methodology for assessing it, has remained unknown. As a result, it is a fully open subject that is still being investigated today (Dang-Van, 1993).

There are two forms of multiaxial loading: proportional and non-proportional. The first form of loading does not modify the primary stress directions since the loads are in phase.

However, in non-proportional loading, these directions are constantly changing due to out-of-phase loads Figure 2.5. Since these two forms of loading produce distinct fatigue behaviours, the models developed for proportional loading are often inapplicable to the second. Furthermore, non-proportional loading is often more detrimental and requires a more sophisticated interpretation and forecast of fatigue life (Kamal & Rahman, 2018).

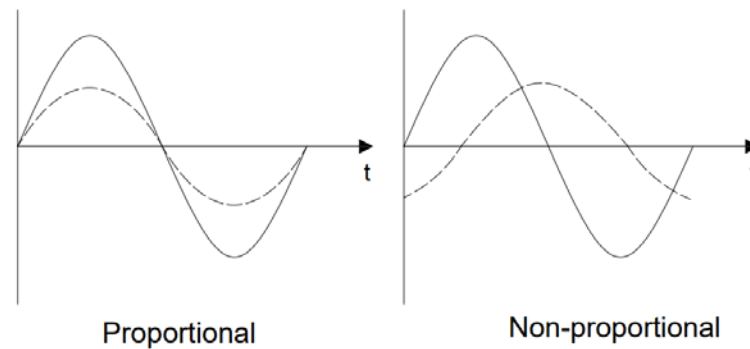


Figure 2.5 Proportional and non-proportional loading.

### 2.3 Multiaxial Fatigue Models

As previously mentioned, since multiaxial fatigue is a complicated phenomenon, it should not be reduced to a simple static or equivalent uniaxial fatigue condition. Indeed, a vast number of factors must be considered, including the material's cyclic characteristics and the distinct impacts of shear and normal stress (Margetin et al., 2016).

As a result, a significant variety of multiaxial fatigue models accounting for various aspects have evolved throughout the previous century. In general, each model attempts to represent the multiaxial fatigue process and damage in a mathematically consistent manner. Since the creation of multiaxial fatigue models is a relatively new and unexplored field, a huge variety of models and divergent viewpoints may readily be discovered in the literature. Frequently, contradicting concepts are expressed, making it difficult to develop a thorough understanding of multiaxial fatigue. Consequently, it was determined to address this subject from the most widely acknowledged and discussed perspectives. Since the creation of multiaxial fatigue models is a relatively young and open issue, a wide variety of models and divergent points of view may readily be found in the literature. Frequently, even contradictory concepts are expressed, making it difficult to develop a thorough understanding of multiaxial fatigue. As a result, it was determined to

approach this subject from the most often acknowledged and cited perspectives (Lee et al., 2011).

The stress-based models are based on the principal stresses and are well suited to the high cycle regime since it is except as an elastic deformation state. Stain models, on the other hand, are based on the strain tensor and are often used in the low cycle regime. They are, however, equally suited for the high-cycle fatigue regime, which makes them an excellent option for assessing both regimens. Finally, the energy models are quantitative in nature and relate to plastic deformation energy. As a result, they are more suited to being adapted to low-cycle regimes (Maktouf et al., 2016).

Method section will discuss some of the most significant and influential models developed during the previous several decades.

#### **2.4 A Review of existing multiaxial fatigue tests**

Numerous structures and equipment used in modern engineering, such as aeronautical aircraft, nuclear reactors, pressure vessels, vehicle crankshafts, turbine rotor vanes, machine tool spindles, and other critical structural components, are often exposed to multiaxial loads. However, in the early years, complicated multiaxial stress was similar to uniaxial stress based on static strength theory, and multiaxial fatigue issues were subsequently addressed using uniaxial fatigue theory. Although this approach is efficient for multiaxial proportional loads, it is ineffective for multiaxial non-proportional loads, which are more comparable to real loads. In comparison to uniaxial fatigue, multiaxial fatigue is more complex in terms of experimental study, physics mechanism, and mechanics analysis.

The following are the experiences that will be discussed in this research:

- Fatigue life estimation of steel half-pipes bolted connections for onshore wind towers applications (Dantas, 2019).
- Analytical and experimental studies on fatigue crack path under complex multi-axial loading (Reis et al., 2006).
- Multiaxial fatigue life prediction for titanium alloy TC4 under proportional and nonproportional loading (Wu et al., 2014)

- Evaluation of Multiaxial Fatigue Life Prediction Methodologies for Ti-6Al-4V (Kallmeyer et al., 2002).
- A multi-axial and high-cycle fatigue life prediction model based on critical plane criterion (Yang et al., 2022).

The Dantas (2019) master's thesis was written with the following aims in mind:

- Perform uniaxial and biaxial fatigue tests at different stress ratios to characterize the fatigue behaviour of S355 steel in the high cycle zone.
- Determine experimental uniaxial and multiaxial fatigue curves for S355 steel at different stress ratios.
- Evaluate several multiaxial fatigue damage models and select the one that best describes the fatigue behaviour of S355 steel.
- Create a numerical fatigue curve for bolted steel half-pipe connectors used in onshore wind turbines.

In addition to testing S355 steel for fatigue and fracture, the main mechanical and chemical properties of the steel must be found and characterized. Most of the information was provided by the material producer.

Table 2.1 Mechanical properties (Dantas, 2019).

| <b>Young<br/>Modulus E<br/>GPa</b> | <b>Yield<br/>Strength <math>f_y</math><br/>MPa</b> | <b>Tensile<br/>Strength <math>f_u</math><br/>MPa</b> | <b>Hardness<br/>HV10</b> |
|------------------------------------|--|--|--------------------------|
| 211.60                             | 367  | 579  | 151.28                   |

Table 2.2 Chemical composition (Dantas, 2019).

| <b>C %</b> | <b>Cu %</b> | <b>Mn %</b> | <b>N %</b> | <b>P %</b> | <b>S %</b> | <b>Si%</b> |
|------------|-------------|-------------|------------|------------|------------|------------|
| 0.16       | 0.2         | 1.28        | 0.009      | 0.03       | 0.02       | 0.3        |

Apart from mechanical and chemical descriptions, it is critical to inspect and analyse the microstructure of the material. As a result, a piece of material was polished and etched with nitric acid to enable the inspection of the microstructure. The outcome of this operation is shown in Figure 2.7. As anticipated for an S355 steel, pearlite and ferrite are present in the microstructure, but the grain edges are sharp, indicating that the material was not normalized. Even though this is not a conventional procedure, it should have no effect on tiredness-related behaviour (Dantas, 2019).

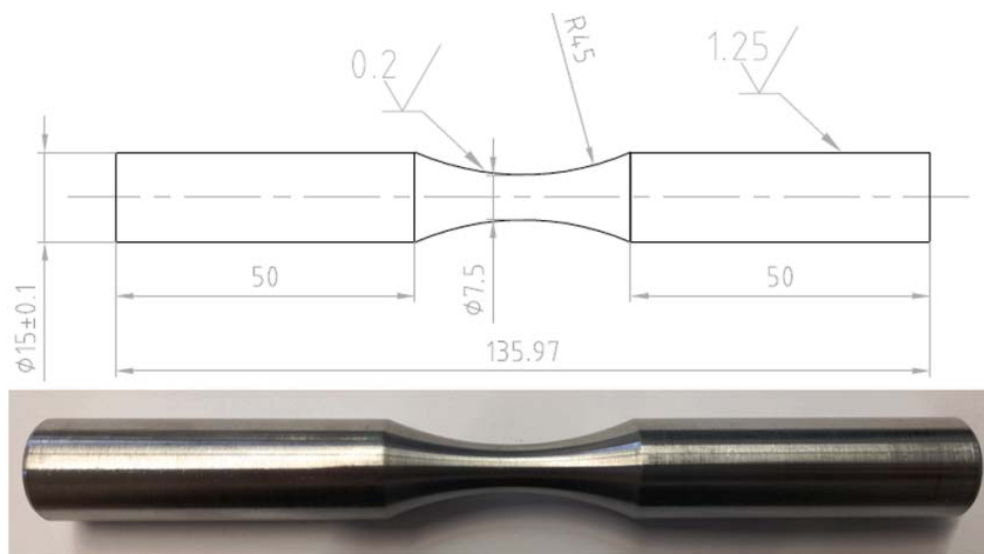


Figure 2.6 Hourglass specimen (in mm) (Dantas, 2019).



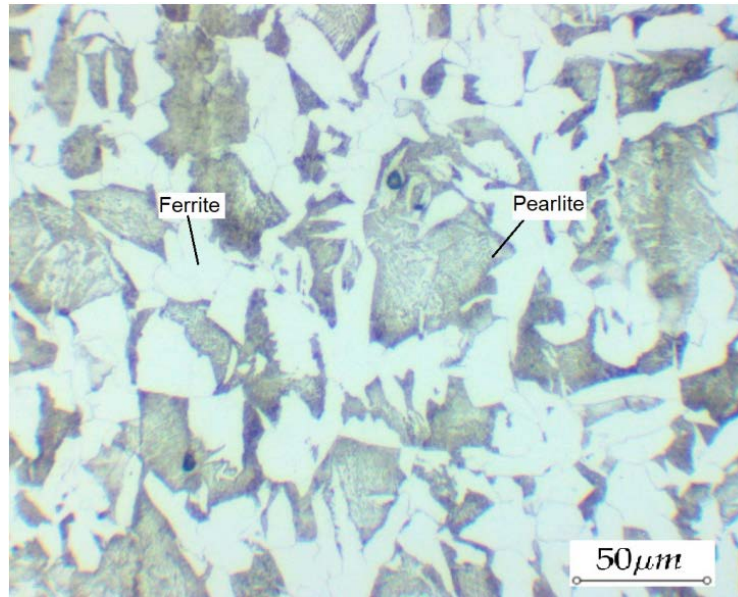


Figure 2.7 Microstructure of S355 steel (Dantas, 2019).

Since the purpose of this study is to determine the fatigue behaviour of S355 structural steel in the high-cycle fatigue regime, experimental findings were analysed and evaluated using stress-based models. These models may be classified according to their empirical, critical plane models or equivalent stress. The empirical models were initially built based on experimental fatigue data. Based on static yield requirements, equivalent stress models convert a multiaxial fatigue stress condition to an equivalent uniaxial stress state (Kallmeyer et al., 2002).

Finally, critical plane models are based on the idea of a critical plane, which is defined as a region with a greater risk of fracture initiation. Five multiaxial fatigue models were investigated and applied to the experimental data gained in this work: Sines, Findley, McDiarmid, Dang Van, and Susmel (Dantas, 2019).

A specified and executed experimental campaign was designed with the goal of collecting mean fatigue curves and analysing each multiaxial fatigue model. As a result, uniaxial and biaxial fatigue tests on smooth hourglass specimens constructed of S355 structural steel with a minimum cross section of  $44.18 \text{ mm}^2$  were conducted Figure 2.6. Tables 2.1 and 2.2 detail the mechanical properties and chemical compositions of the S355 steel that was tested. The hardness was assessed and quantified using a sample cut from a specimen. Additionally, the microstructure was analysed, revealing a ferrite-pearlite microstructure, as seen in Figure 2.7.

As a result, nineteen uniaxial and eighteen biaxial fatigue tests were done at two stress ratios:  $R = 0.01$  and  $R = 1$ . A cyclic axial force was supplied to the specimen during axial testing, while biaxial tests applied both a cyclic axial force in phase and a cyclic torsional torque. In sixteen biaxial tests, the shear stress induced by the torque was half that caused by the force, while the normal stress caused by the force was equal in the remaining tests, to determine the influence of shear stress on fatigue life. The stresses were delivered at a 10 Hz frequency using sinusoidal functions with constant amplitude across time.

Both types of tests were conducted under force control, using an MTS 810 axial testing system capable of applying a maximum axial force of 100kN for axial tests and an MTS 809 axial/torsional testing system capable of applying a maximum axial force of 50kN and a maximum torsional force of 0.5kN for biaxial tests. The number of cycles required to reach failure and the degree of loading applied were recorded for each test. Due to the limited amount of material, only two experimental experiments were conducted for each loading level. It was considered that the specimen had run out and the test was terminated after 5,000,000 cycles had been completed without the specimen failing (Dantas, 2019).

Another experiment was done by Reis et al. (2006), this experiment investigates the impact of multi-axial loading direction on crack path. The aim of this research is to examine and compare two materials: AISI 303 stainless steel and 42CrMo4 steel.

Experiments were done on an INSTRON 8800 biaxial tester. Six distinct biaxial loading pathways were chosen and used in the experiments to determine the impact of multiaxial loading paths on the additional hardening, fatigue life, and the direction of fracture propagation. Optical microscopy and SEM techniques were used to perform fractographic investigations of the plane orientations of crack initiation and propagation (Reis et al., 2006).

Tables 2.3 and 2.4 provide, respectively, the monotonic mechanical characteristics and chemical composition. The geometry and dimensions of the specimens utilised in the testing programme are shown in Figure 2.8. Prior to testing, the specimens were polished.

To describe the cyclic stress–strain behaviour of the investigated materials, tension–compression low cycle fatigue experiments were conducted.

Table 2.3 Monotonic and cyclic mechanical properties (Reis et al., 2006).

| <b>Monotonic and cyclic mechanical properties</b> |                |                 |
|---|----------------|-----------------|
|   | <b>42CrMo4</b> | <b>AISI 303</b> |
| <b>Tensile strength<br/>(MPa)</b>                 | 1100           | 625             |
| <b>Yield strength<br/>(MPa)</b>                   | 980            | 330             |
| <b>Elongation %</b>                               | 16             | 58              |
| <b>Young's modulus<br/>(GPa)</b>                  | 206            | 178             |
| <b>Cyclic yield strength<br/>(MPa)</b>            | 640            | 310             |
| <b>Strength coefficient<br/>(MPa)</b>             | 1420           | 2450            |
| <b>Strain hardening<br/>exponent</b>              | 0.12           | 0.35            |
| <b>Fatigue strength<br/>coefficient (MPa)</b>     | 1154           | 534             |
| <b>Fatigue strength<br/>exponent</b>              | -0.061         | -0.07           |
| <b>Fatigue ductility<br/>coefficient</b>          | 0.18           | 0.052           |
| <b>Fatigue ductility<br/>exponent</b>             | -0.53          | -0.292          |

Table 2.4 Chemical compositions of the materials studied in (wt%) (Reis et al., 2006).

|                 | <b>C</b> | <b>Si</b> | <b>Mn</b> | <b>P</b> | <b>S</b> | <b>Cr</b> | <b>Ni</b> | <b>Mo</b> | <b>Cu</b> |
|-----------------|----------|-----------|-----------|----------|----------|-----------|-----------|-----------|-----------|
| <b>42CrMo4</b>  | 0.39     | 0.17      | 0.77      | 0.025    | 0.020    | 1.10      | 0.20      | 0.16      | 0.21      |
| <b>AISI 303</b> | 0.12     | 1.00      | 2.00      | 0.060    | 0.25     | 18.00     | 9.00      | ---       | ---       |

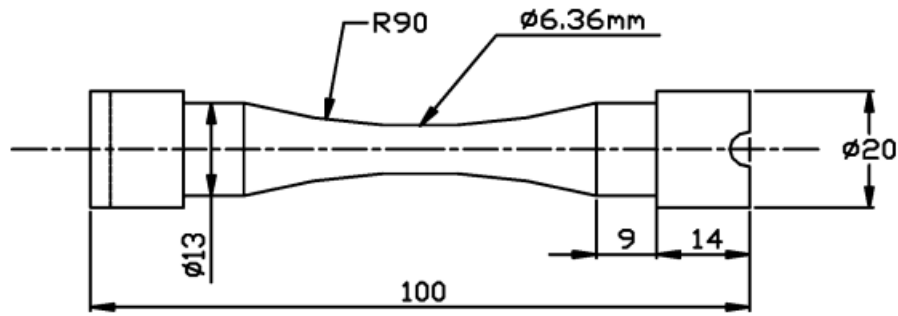


Figure 2.8 Specimen geometry for biaxial cyclic tension–compression with cyclic torsion tests (Reis et al., 2006).

According to Wu et al. (2014) a tubular specimens of titanium alloy TC4 were subjected to both proportional and asymmetric tension–torsion fatigue testing. Six multiaxial fatigue parameters are analysed and assessed in conjunction with test-obtained data on service life. Due to the excellent strength and stiffness to weight ratio of titanium alloys, they are used in several sectors, including aerospace. This material's components and structures, such as turbine engine blades and rotors, are consistently exposed to multiaxial stresses. The purpose of this research is to investigate the multiaxial fatigue behaviour of titanium alloy TC4 and to identify appropriate multiaxial fatigue models for predicting the fatigue life of this material. TC4 is the trademark for titanium alloy in China. In America, the equivalent substance is Ti–6Al–4V (Wu et al., 2014).

The material's chemical composition is shown in Table 2.5. The material was heated to 730 degrees Celsius for 1.5 hours before being cooled by air. Figure 2.9 depicts the typical microstructure of the alloy. Solid specimens with a 5 mm diameter and a 30 mm gauge length for monotonic testing and a 6 mm diameter and a 15 mm gauge length for axial fatigue tests were machined from solid bars with a diameter of 35 mm. For pure torsional and multiaxial fatigue testing, the same bars were also machined into tubular specimens with a 17 mm outer diameter, a 14 mm internal diameter, and a 32 mm gauge length in accordance with ASTM standard E2207. Figure 2.10 depicts the configuration and size of tubular specimens. A servo-hydraulic MTS Model 809 axial–torsion testing system underwent fatigue tests. All fatigue tests, including axial, torsion, in-phase, 45 out-of-phase, and 90 out-of-phase, were conducted using totally reversed sinusoidal waveforms of 0.5–1.0 Hz frequency. The control modes for axial and torsion,

respectively, were displacement and angle. Using an axial–torsion extensometer, axial and shear stresses were measured. In addition, axial load and torque were observed. The failure threshold was 10 to 15% load or torque loss compared to midlife stable values (Wu et al., 2014).

Table 2.5 The chemical composition of TC4 (wt%) (Wu et al., 2014)

| <b>Al</b> | <b>V</b> | <b>Fe</b> | <b>C</b> | <b>N</b> | <b>H</b> | <b>O</b> | <b>Ti</b> |
|-----------|----------|-----------|----------|----------|----------|----------|-----------|
| 6.4       | 4.1      | 0.2       | 0.01     | 0.01     | 0.002    | 0.16     | Balance   |

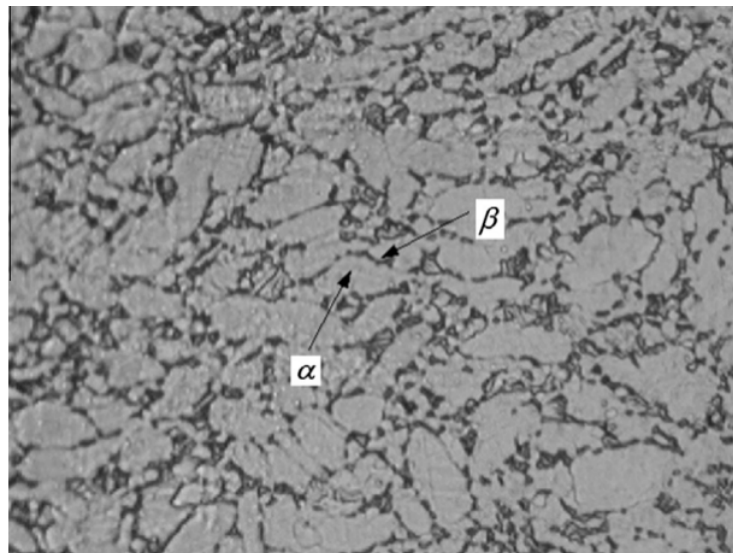


Figure 2.9 Microstructure typical of titanium alloy TC4 (Wu et al., 2014).

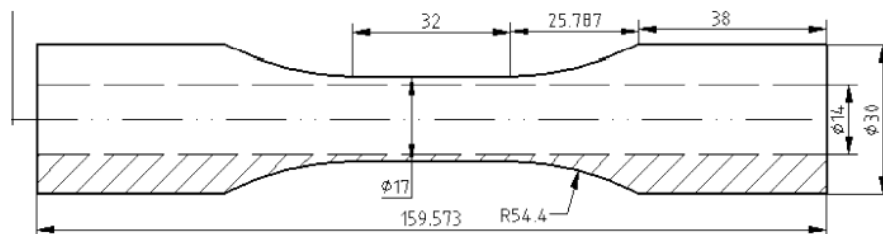


Figure 2.10 Specimen geometry (Wu et al., 2014).

Table 2.6 shows the titanium alloy TC4's monotonic properties and axial and shear fatigue parameters. The cyclic stress–strain characteristics are listed in table 2.6 as well. All the information was obtained at a cycle of 0.5Nf.

Table 2.6 Fatigue and cyclic stress–strain properties of titanium alloy TC4 (Wu et al., 2014).

|                             |                                     |                         |                                    |                           |                                |                          |
|-----------------------------|-------------------------------------|-------------------------|------------------------------------|---------------------------|--------------------------------|--------------------------|
| <b>Monotonic properties</b> | <b>E (GPa)</b>                      | <b>G (GPa)</b>          | <b><math>\sigma_y</math> (MPa)</b> | <b><math>\nu_e</math></b> | <b>K (MPa)</b>                 | <b>n</b>                 |
|                             | 108.4                               | 43.2                    | 942.5                              | 0.25                      | 1054                           | 0.0195                   |
| <b>Uniaxial properties</b>  | <b><math>\sigma'_f</math> (MPa)</b> | <b>b</b>                | <b><math>\epsilon'_f</math></b>    | <b>c</b>                  | <b><math>K'</math> (MPa)</b>   | <b><math>n'</math></b>   |
|                             | 1116.9                              | -0.049                  | 0.579                              | -0.679                    | 1031                           | 0.0478                   |
| <b>Torsional properties</b> | <b><math>\tau'_f</math> (MPa)</b>   | <b><math>b_0</math></b> | <b><math>\gamma'_f</math></b>      | <b><math>c_0</math></b>   | <b><math>K'_0</math> (MPa)</b> | <b><math>n'_0</math></b> |
|                             | 716.9                               | -0.06                   | 2.24                               | -0.8                      | 446.7                          | 0.016                    |

Kallmeyer et al. (2002) conducted another multiaxial experiment in which T1 was used for this investigation. The purpose of Kallmeyer et al. (2002) research was to discover multiaxial fatigue models that may be used to estimate the service life of modern monolithic materials, such as those utilised in aviation engine and airframe applications. Existing multiaxial fatigue models, including both equivalent-stress and critical-plane techniques, are examined for their applicability to multiaxially loaded Ti-6Al-4V. Ti-6Al-4V encounters primarily elastic cyclic deformations in the majority of applications.

Typical service load ratios are often zero or positive, so there is frequently just flexibility on the first reversal. Even at fatigue lifetimes of  $10^3$  to  $10^4$  cycles, the cyclic plastic stresses are minimal or insignificant compared to the elastic components (Kallmeyer et al., 2002).

Ti-6Al-4V specimens with a smooth surface were subjected to biaxial tension and torsion fatigue testing with varying load ratios and non-proportionality. For this material, multiaxial fatigue models were assessed based on their ability to correlate biaxial fatigue data with uniaxial fatigue data at varying stress ratios ( $R = \sigma_{min}/\sigma_{max}$ ). The effect of mean stresses under multiaxial loading circumstances, specifically torsional mean stresses, is discussed. The processes linked with massive crack formation were not

examined in this work. It was considered that the damage parameters assessed here reflect the combined impacts of fracture nucleation and advancement.

The Ti-6Al-4V material utilised in this investigation was forged from 6.4 cm bar stock into about 40 cm x 15 cm x 20 mm plates. The chemical composition of the first billet is shown in Table 2.7, and Table 2.8 lists the material characteristics utilised in the study. The forgings were then solution-treated at a temperature of 932 °C to achieve a homogeneous microstructure. The forgings were fan-cooled and mill-annealed at 704 °C for two hours after solution treatment. About 60% of the microstructure of the forgings was made up of primary alpha phase, while the rest was made up of lamellar converted beta phase (Kallmeyer et al., 2002).

Table 2.7 Chemistry of the material Ti-6Al-4V (Kallmeyer et al., 2002).

| <b>Al %</b> | <b>V %</b> | <b>Fe %</b> | <b>O %</b> | <b>N%</b> | <b>Ti</b> |
|-------------|------------|-------------|------------|-----------|-----------|
| 6.3         | 4.2        | 0.2         | 0.18       | 0.012     | Balance   |

The biaxial test specimens were machined in the longitudinal 40 cm direction from the forged plates. To minimise residual tensions and surface damage, the specimens were low-stress ground and longitudinally polished, stress relief annealed for one hour at 704°C in a vacuum, then chem milled with nitric-hydrofluoric acid. Tests were conducted on solid specimens with a grip diameter of roughly 19 mm, a gauge section diameter of 12.5 mm, and a length of 30 mm. A tubular specimen was explored for this project, but it was rejected since it lacked the requisite thin wall thickness of less than 1 mm. The biaxial fatigue tests were done at room temperature on a servo hydraulic tension-torsion load frame with axial load capacities of 445 kN and 5000 N-m. Strains were measured using a modified MTS model 632.85 biaxial extensometer that contacted the specimen with conical ends. The modification to the extensometer entailed strain-gauging the existing flexure components in order to detect torsional stresses. All experiments were conducted under strain control at frequencies between 0.5 and 2 Hz (Kallmeyer et al., 2002).

Table 2.8 Material Properties for Ti-6Al-4V (Kallmeyer et al., 2002).

|   |        |
|---|--------|
| <b>Modulus of elasticity E (GPa)</b>                        | 116    |
| <b>Cyclic strain hardening coefficient K' (MPa)</b>         | 854    |
| <b>Cyclic strain hardening exponent n'</b>                  | 0.0149 |
| <b>Cyclic yield strength <math>\sigma_y'</math> (MPa)</b>   | 750    |
| <b>Monotonic yield strength <math>\sigma_y</math> (MPa)</b> | 930    |
| <b>Ultimate strength <math>\sigma_{ut}</math> (MPa)</b>     | 977    |

It is essential for engineering applications to accurately estimate the fatigue failure behaviour and fatigue life of structures or materials subjected to multiaxial loads. In Yang et al. (2022) research, a multiaxial and high-cycle fatigue failure model based on the critical plane criteria is presented, considering the effects of material property and loading route on the onset and development of fatigue cracks. The mechanical properties of a material are described by the ratio of its tensile yield strength  $\sigma_y$  and its torsional yield strength  $\tau_y$ . For  $\sigma_y / \tau_y < \sqrt{3}$ , it is believed that the maximum normal stress controls the fracture propagation under the multi-axial fatigue load. For  $\sigma_y / \tau_y > \sqrt{3}$ , it is thought that the maximum shear stress controls how the crack spreads when a multi-axial fatigue load is applied. Three types of materials experimental data were used to validate the model. Most fatigue life predictions for all materials fall within the  $\pm 2$ -time scatter range, whereas just a few data points fall within the  $\pm 3$ -time scatter band. Good correlations between the predicted fatigue life of the model and experimental findings demonstrated the usefulness of the concept. The model offers a valuable tool for forecasting the multiaxial fatigue life of materials under various loading settings (Yang et al., 2022).

Currently, the development of a multi-axial fatigue failure criteria is mostly focused on the critical plane-based criterion. This criterion posits that fatigue failures occur on a certain plane and uses the combination of several stress components on this plane to assess failure. Various loading parameter implications are evaluated, but this criterion cannot accommodate all loading routes. In addition, insufficient research on fracture



initiation and development behaviour under multi-axial stress necessitates a substantial increase in efforts to identify the critical plane under multi-axial high cycle fatigue loading. In addition, there is no mature, generally recognised failure criteria and life forecast approach for multiaxial and high-cycle fatigue. Consequently, the purpose of this study is to develop a novel failure prediction model based on the critical plane criteria and to verify the model by comparing its predictions to experimental data (Yang et al., 2022). The three used materials are SM45C, SAE1045, and LY12CZ. In Table 2.9, the mechanical parameters of the used materials are summarised and reported.

Table 2.9 Mechanical parameters of various materials (Yang et al., 2022)

|                                 | Mechanical properties |            | Parameters of tension S-N curve |          |                      | Parameters of torsion S-N curve |          |                      |
|---------------------------------|-----------------------|------------|---------------------------------|----------|----------------------|---------------------------------|----------|----------------------|
|                                 | $\sigma_y$            | $\sigma_u$ | $\sigma_f$                      | <b>b</b> | <b>R<sup>2</sup></b> | $\tau_f$                        | <b>C</b> | <b>R<sup>2</sup></b> |
| <b>SM45C</b>                    | 447                   | 662        | 1024                            | -0.094   | 0.97                 |                                 | -0.048   |                      |
| <b>SAE1045(tension/torsion)</b> | 310                   | 565        | 481                             | -0.1406  | 0.99                 | 330                             | -0.127   | 0.98                 |
| <b>LY12CZ</b>                   | 275                   | 415        | 1143                            | -0.1400  | 0.99                 | 565                             | -0.112   | 0.99                 |
| <b>SAE1045(bending/torsion)</b> | 310                   | 565        | 1765                            | -0.1582  | 0.96                 | 492                             | -0.078   | 0.98                 |

### 3 Method

The fatigue damage parameters and strategy of multiaxial fatigue techniques are typically classified. Methods based on the critical plane are seen as promising for the investigation of multiaxial fatigue issues since they correlate well with experimental results. In addition, they may include non-proportionality and differentiate between phase shift-induced and frequency-induced non-proportionality. Experimentally, fatigue crack initiation (i.e., nucleation and early growth) seems to occur on selected material planes. Consequently, several crucial plane-based approaches were first established for smooth and notched specimens, and several crucial plane-based approaches have been developed or expanded recently.

#### 3.1 Conventional Methods:

The fatigue phenomenon was originally identified around the end of the nineteenth century, and August Wohler was one of the first to describe it. He not only presents the results of many fatigue experiments, but also made significant conclusions regarding them, such as the following: the primary parameter influencing fatigue life is the stress amplitude, whereas the mean stress has a minor effect. Basquin continued Wohler's work a few years later by developing a method for representing and evaluating fatigue life that is still very relevant today (Schütz, 1996).

This section will introduce and discuss Basquin's work, as well as other significant fatigue techniques established during the previous century. The models presented in this chapter assume that the original material is flawless and free of cracks or defects. If a detailed analysis of a material's response to the existence of a defect or the stage of crack propagation is necessary, a mechanic fracture technique should be used (Lee et al., 2011).

##### 3.1.1 S-N Curves

Basquin proposed plotting the fatigue data points as stress amplitude  $\sigma_a$  vs. number of cycles to failure  $N_f$ , with the number of cycles axis set to a logarithmic scale and the stress amplitude axis set to a logarithmic or linear scale Figure 3.1. Thus, a linear curve known as the S-N curve or Wohler curve may be obtained. As a mean curve, the S-N curve reflects each combination of stress amplitude and cycle number for which half of the specimens fail. It is important to mention that there is an S-N curve for each value of

mean stress, and that this curve is situated lower on the graph for greater values of mean stress (Hudok, 1990).

The S-N curve can be expressed as:

$$\sigma_a = \sigma_f (2N_f)^b \quad (3.1)$$

Where,  $\sigma_f$  is the fatigue strength at one cycle, and  $b$  is a material constant and the linear regression slope.

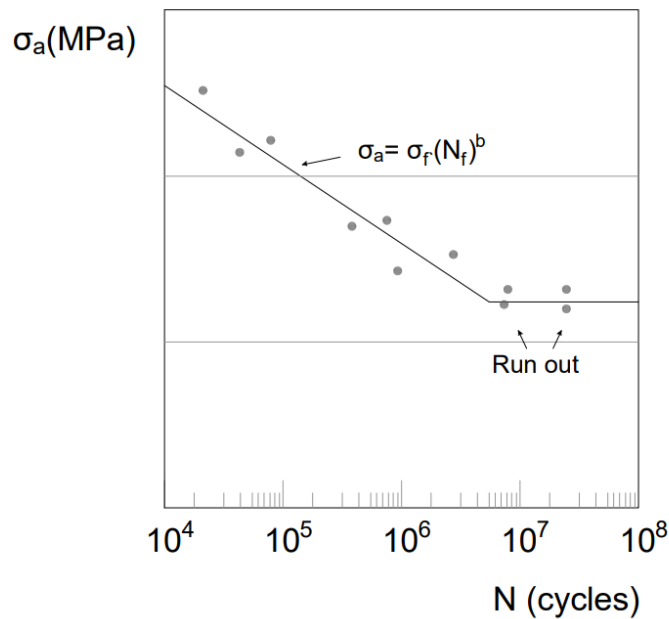


Figure 3.1 S-N curve (Schijve, 2003).

The S-N curve for a material may be determined by conducting an experimental campaign using unnotched specimens. Since the initiation stage represents around 90% of each specimen's fatigue life, this curve can also be used to estimate the initiation fracture stage of a notched element (Schijve, 2003).

### 3.1.2 Fatigue curve:

Fatigue diagrams provide fatigue data in a single curve for a set number of cycles or for the fatigue limit. Typically, this curve reflects the amplitude stress, the minimum or maximum stress as a function of the mean stress and may be compared to the S-N curves Figure 3.2. Furthermore, all curves converge to the ultimate tensile strength or yield strength when the amplitude stress is equal to zero (Schijve, 2003).

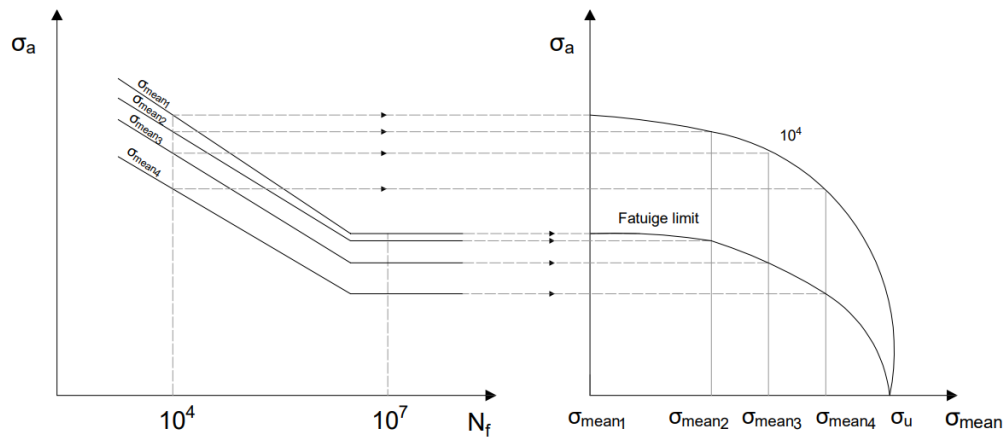


Figure 3.2 Fatigue diagram as a cross plot of S-N curves (Schijve, 2003).

This is a generic definition of this form of representation, although each diagram type certainly has some differences. In the following sections, the most relevant fatigue diagrams will be discussed.

### 3.1.2.1 Gerber

Gerber introduced the following equation as a fatigue criteria in about 1880:

$$\sigma_a = \sigma_{f0-1} \left( 1 - \left( \frac{\sigma_{mean}}{\sigma_u} \right)^2 \right) \quad (3.2)$$

Where  $\sigma_u$  is the ultimate tensile strength and  $\sigma_{f0-1}$  is the fatigue limit for  $R = -1$ .

As seen in Figure 3.3, this picture is a parabola that takes the fatigue limit and ultimate strength into account.

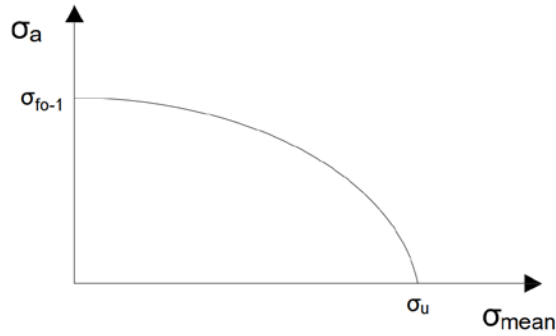


Figure 3.3 Gerber fatigue limit

### 3.1.2.2 Goodman

A few years later, in 1900, Goodman presented the formula from Equation 2.6 as a criterion. However, this figure has been changed to include a second condition that avoids the plastic deformation zone. This pair of equations is referred to as the "modified Goodman" pair, and it is represented by the system Equation 3.4.

Figure 3.4 illustrates the original and amended Goodman diagrams. Thus, the safety area is decreased from the original to the updated figure, as it arises from the junction of regions under the two prescribed lines.

$$\sigma_a = \sigma_{f0-1} \left(1 - \frac{\sigma_{mean}}{\sigma_u}\right) \quad (3.3)$$

$$\left. \begin{aligned} \sigma_y &= \sigma_{mean} + \sigma_a \\ \sigma_a &= \sigma_{f0-1} \left(1 - \frac{\sigma_{mean}}{\sigma_u}\right) \end{aligned} \right\} \quad (3.4)$$

Where  $\sigma_y$  is a normal stress in the direction of y-axis.

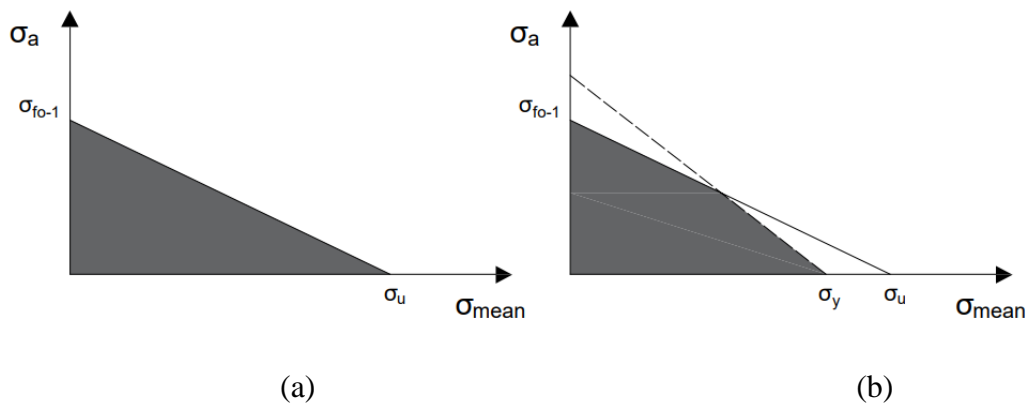


Figure 3.4 Goodman fatigue diagram (a) Goodman fatigue diagram and (b) Modified Goodman fatigue diagram

### 3.1.2.3 Soderberg

The Soderberg diagram, developed in about 1930, is the most cautious and safest since it restricts the maximum mean stress value to the yield strength. As a result, the following linear relation is proposed as a fatigue criterion:

$$\sigma_a = \sigma_{fo-1} \left(1 - \frac{\sigma_{mean}}{\sigma_y}\right) \quad (3.5)$$

The Soderberg form in Figure 3.5 enables the linear relationship between  $\sigma_a$  and  $\sigma_{mean}$  to be verified.

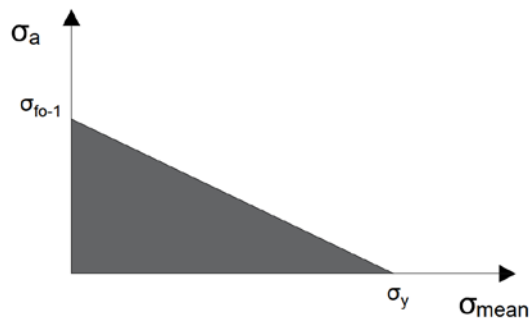


Figure 3.5 Soderberg fatigue diagram

## 3.2 Multiaxial Fatigue Models

### 3.2.1 Stress Based Multiaxial Fatigue Models

Apart from the categorization stated above, there are many types of stress-based models: equivalent stress, empirical formula, and critical plane models (Lee et al., 2011). Each of these classifications has unique properties that will be discussed. The models are as following:

### 3.2.2 Models Based on Empirical Formulas

Empirical models were the first to emerge and are well correlated with experimental fatigue results. The primary limitation of these models is their inability to apply to biaxial totally reversed stress states (Lee et al., 2011).

### 3.2.3 Gough and Pollard Model

Gough and Pollard performed a significant number of in-phase fatigue experiments under bending and torsional stresses in the 1930s, which enabled the creation of an empirical model in 1950. Different failure conditions for brittle and ductile materials are established by the given hypothesis:

$$\left(\frac{\sigma_a}{\sigma_{a,R=-1}}\right)^2 + \left(\frac{\tau_a}{\tau_{a,R=-1}}\right)^2 = 1 \quad (3.6)$$

where  $\sigma_{a,R=-1}$  represents the completely reversed fatigue limit for pure bending and  $\tau_{a,R=-1}$  represents the fully reversed fatigue limit for pure torsion (Lee et al., 2011).

### 3.2.4 Models of Equivalent Stress

The models of equivalent stress are based on static yield requirements and are used to convert a multiaxial condition to an equivalent uniaxial fatigue stress state. Many of these models are incapable of being applied to non-proportional loads and are ineffective at including fatigue phenomena. However, they are often used because they are simple and easy to use (Kallmeyer et al., 2002).

### 3.2.5 Maximum Principal Stress Model

According to the maximum principal stress model, fatigue crack initiation occurs when the maximum principal stress amplitude  $\sigma_{1,a}$  is equal to or larger than the uniaxial

completely reversed test's normal stress fatigue limit  $\sigma_{a,R=-1}$ . The maximum principal stress damage parameter is  $\sigma_E$ .

$$\sigma_E = \sigma_{a,R=-1} \leq \sigma_{1,a} \quad (3.7)$$

### 3.2.6 Maximum Shear Stress (Tresca)

The Tresca criteria can also be applied to fatigue, with the assumption that the starting crack occurs when the following conditions are met.

$$\tau_E = \tau_{a,\max} = \frac{\sigma_{1,a} - \sigma_{3,a}}{2} \leq \tau_{a,R=-1} \quad (3.8)$$

Where  $\sigma_{1,a}$  represent the maximum principal amplitude,  $\sigma_3$  is the minimum principal amplitude,  $\tau_{a,\max}$  is the maximum shear stress amplitude and  $\tau_{a,R=-1}$  is the uniaxial torsional fatigue stress limit amplitude for  $R = -1$  (Lee et al., 2011).

### 3.2.7 Von Mises Model

The von Mises model applied to fatigue states that the fracture initiates when Equation (3.9) is

$$\sigma_{VM,m} * \sigma_{VM} + \sigma_{VM,a} \geq \sigma_{a,R=-1} \quad (3.9)$$

Where,  $\sigma_{VM,m}$  is the von Mises mean stress.  $\sigma_{VM}$  is the mean stress sensitivity factor, and  $\sigma_{VM,a}$  represent the von Mises stress amplitude.

$\sigma_{VM,a}$  and  $\sigma_{VM,m}$  can be calculated as following:

$$\sigma_{VM,a} = \frac{1}{\sqrt{2}} \sqrt{(\sigma_{1,a} - \sigma_{2,a})^2 + (\sigma_{2,a} - \sigma_{3,a})^2 + (\sigma_{1,a} - \sigma_{3,a})^2} \quad (3.10)$$

$$\sigma_{VM,m} = \sigma_{1,\text{mean}} + \sigma_{2,\text{mean}} + \sigma_{3,\text{mean}} \quad (3.11)$$

where  $\sigma_{1,a}$ ,  $\sigma_{2,a}$  and  $\sigma_{3,a}$  are the principal stresses amplitudes and  $\sigma_{1,\text{mean}}$ ,  $\sigma_{2,\text{mean}}$ , and  $\sigma_{3,\text{mean}}$  are the principal mean stresses (Kamal & Rahman, 2018).

### 3.2.8 Sines Model

Sines (1955) performed a thorough investigation of experimental fatigue data for bending, torsional, and combined torsional and bending, which resulted in the formulation of equation 2.15. When the left side of the equation is greater than the constant  $s$ , the failure occurs.



$$k_s (3\sigma_{hmean}) + \tau_{a,oct} = s \quad (3.12)$$

where  $k_s$  is a material constant representing the permissible amount of static stress,  $s$  is a constant material corresponding to the fatigue limit, and  $\sigma_{hmean}$  is the hydrostatic stress for mean stresses defined as:

$$\sigma_{hmean} = \frac{\sigma_{1mean} + \sigma_{2mean} + \sigma_{3mean}}{3} \quad (3.13)$$

where  $\tau_{a,oct}$  is the amplitude of the octahedral shear stress derived using the following equation:

$$\tau_{a,oct} = \frac{1}{3} \sqrt{(\sigma_{1,a} - \sigma_{2,a})^2 + (\sigma_{2,a} - \sigma_{3,a})^2 + (\sigma_{1,a} - \sigma_{3,a})^2} \quad (3.14)$$

Both constants may be determined using two tensile fatigue tests: one with  $R=-1$  and another with  $R=0$ .

$$\tau_{a,oct R=-1} = \frac{\sqrt{2}}{3} \sigma_{a,R=-1} \quad (3.15)$$

$$\sigma_{hmean R=-1} = 0 \quad (3.16)$$

Afterwards, it is obtained:

$$s = \tau_{a,oct R=-1} \quad (3.17)$$

For  $R=0$

$$\tau_{a,oct R=0} = \frac{\sqrt{2}}{3} \sigma_{a,R=0} \quad (3.18)$$

$$\sigma_{hmean R=0} = \sigma_{1mean} = \sigma_{1,a} \quad (3.19)$$

$$k_s = \frac{\sqrt{2}}{3} \left( \frac{\sigma_{a,R=-1} - \sigma_{a,R=0}}{\sigma_{a,R=0}} \right) \quad (3.20)$$

While this model incorporates the impact of mean stress, it cannot be used for nonproportional loading (Lee et al., 2011).

### 3.2.9 Crossland Model

The Crossland model is similar to the Sines model except that it includes the maximum hydrostatic stress, as shown in Equation (3.21). Therefore, this model may be used in situations when the loading is not proportionate.

$$k_c * (3\sigma_{hmax}) + \tau_{a,oct} = c \quad (3.21)$$

where  $k_c$  and  $c$  are material constants, and  $\sigma_{hmax}$  is the maximum hydrostatic stress determined by the following equation:

$$\sigma_{hmax} = \frac{\sigma_{1,max} + \sigma_{2,max} + \sigma_{3,max}}{3} \quad (3.22)$$

### 3.3 Models of critical planes.

The critical plane method presents the idea of a critical plane in which fracture initiation is more possible. These models should include the physical mechanisms behind fatigue damage and microcracking, and each model is defined by its critical plane specification (Kallmeyer et al., 2002; McDowell & Ellis, 1993). These models are listed as following:

#### 3.3.1 The Fatemi and Socie critical plane model

Fatemi and Socie introduced the critical plane concept in 1988. The model is as follows:

$$\frac{\Delta\gamma}{2} \left( 1 + k \frac{\sigma_{n,max}}{\sigma_{yield}} \right) = \frac{\tau_f}{G} (2N)^{b\gamma} + \gamma_f (2N)^{c\gamma} \quad (3.23)$$

The shear strain range  $\Delta\gamma$  and the maximum normal stress  $\sigma_{n,max}$  in a plane are the two parameters considered in this model. Shear loading is required for crack initiation since fatigue cracks begin on high-shear planes. Normal stress is also significant, according to Equation 3.23. A positive normal stress lengthens the distance between the structure's atomic planes, allowing shear loading to produce damage. Negative normal stress has the opposite effect (Kristina, 2007).

$$\frac{\Delta\gamma}{2} \left( 1 + k \frac{\sigma_{n,max}}{\sigma_{yield}} \right) = \text{effective shear strain amplitude.}$$

Where,  $\tau_f$  is the coefficient of shear fatigue strength.

$b\gamma$  is the exponent of shear fatigue strength.

$\gamma_f$  is the ductility coefficient of shear fatigue strength.

$c\gamma$  is the exponent coefficient of shear fatigue strength.

$G$  is the shear modulus.

$K$  is a normal stress sensitivity parameter

### 3.3.2 McDiarmid Model

McDiarmid introduced a critical plane method to multiaxial high-cycle fatigue that is applicable to non-proportional loading and considers the mean stress effect.

According to these criteria, the critical plane is defined as the plane in which the shear stress amplitude reaches its highest value. This model distinguishes two distinct scenarios: case A, in which fractures develop parallel to the surface, and case B, in which cracks grow inward from the surface (Kallmeyer et al., 2002).

$$\tau_{A,B} = \tau_{\theta a} + \frac{\tau_{A,B}}{2\sigma_u} \sigma_{\theta \max} \quad (3.24)$$

Where  $\tau_{A,B}$  represent case A and case B for the reversed shear fatigue limit,  $\tau_{\theta a}$  is the alternating shear stress on a  $\theta$  plane.

### 3.3.3 Findley Model

For the first time, Findley (1958) suggested a critical plane strategy. According to these criteria, shear stress is the main mechanism causing fatigue damage, whereas normal stress acts as a secondary mechanism. Thus, shear stress is responsible for the nucleation and initiation of tiny fractures, while normal stress impacts a material's capacity to tolerate cyclic loading. This model incorporates the impact of mean stress, stating that although this variable is insignificant for torsion in ductile metals, it has a significant effect on bending (Findley, 1959).

The critical plane is defined by this criterion as the plane in which a certain damage parameter reaches its greatest value. This equation shows that when the damage

parameter meets the material constant  $f$ , the failure is caused by damage to the material.

$$(k_f * \sigma_{\theta\max} + \tau_{\theta a})_{\max} = f \quad (3.25)$$

Where  $k_f$  and  $f$  are constants for the number of cycles required to reach failure, and  $\sigma_{\theta\max}$  is the maximum normal stress on a  $\theta$  plane.

### 3.3.4 Dang Van Model

Dang-Van proposed a methodology based on "micro-macro" scale analysis and local factors. For engineering purposes, a simpler version of this model was provided (Van Lieshout et al., 2017).

This method establishes that fatigue failure will occur if the following condition is met:

$$d = \tau_{a,\max} + k_d * \sigma_{h,\max} \quad (3.26)$$

Where  $d$  and  $k_d$  are material constants and can be calculated as following:

$$d = \tau_{a,\max} = \tau_{a,R=-1} \quad (3.27)$$

$$k_d = 3 \left( \frac{\tau_{a,R=-1}}{\sigma_{a,R=-1}} - \frac{1}{2} \right) \quad (3.28)$$

Additionally, these constants may be determined by displaying the test data and doing a linear regression on it using two random tests at the fatigue limit (Van Lieshout et al., 2017).

### 3.3.5 Brown and Miller Model

Like the shear and normal stress that Findley recommended for high-cycle fatigue, Miller et al. (1985) argued that both shear and normal strain must be evaluated in the plane of maximal shear. Cyclic shear stresses will aid in the initiation of cracks, whereas normal strain will promote their propagation. Later, Brown and Miller provided a streamlined formulation for cracks:

$$\Delta\gamma = (\Delta\gamma_{\max}^{\alpha} + s \Delta\varepsilon_n^{\alpha})^{\frac{1}{\alpha}} \quad (3.29)$$

Where  $\Delta\gamma$  is the range of equivalent shear strain,  $s$  is a material-dependent quantity that quantifies the effect of normal strain on material crack formation and is calculated by correlating axial and torsion data,  $\Delta\varepsilon_n^a$  is the normal strain amplitude on the maximum shear strain amplitude plane.

### 3.3.6 Smith–Watson–Topper Model

The Smith, Watson, and Topper (SWT) parameter was introduced to assess multiaxial loads for tensile-cracked materials. The plane with the greatest normal strain was selected as the crucial plane. The following describes the format of a SWT parameter:

$$\sigma_{n,max} \frac{\Delta\varepsilon_1}{2} = \frac{\sigma_f^2}{E} (2N_f)^{2b} + \sigma_f \varepsilon_f (2N_f)^{b+c} \quad (3.30)$$

Where  $\sigma_{n,max}$  is the maximum stress on the critical plane,  $\Delta\varepsilon_1$  is the maximum normal strain range,  $E$  is Young's modulus and  $N_f$  is the failure life.  $\sigma_f$ ,  $\varepsilon_f$ ,  $b$  and  $c$  are the fatigue properties.

### 3.3.7 Liu's Virtual Strain Energy Model

Virtual strain energy (VSE) model developed by Liu is an energy-based critical plane model. This model examines two potential failure modes: a tensile failure mode,  $W_I$ , and a shear failure mode,  $W_{II}$ . Failure is anticipated on the material plane with the highest  $V$  value.  $W_I$  is calculated by determining the plane on which the axial work is greatest and then adding the related shear work on the same plane (Liu, 1993).

$$\Delta W_I = (\Delta\sigma_n \Delta\varepsilon_n)_{\Theta}^{max} + (\Delta\tau \Delta\gamma) \quad (3.31)$$

$$\Delta W_{II} = (\Delta\sigma_n \Delta\varepsilon_n) + (\Delta\tau \Delta\gamma)_{\Theta}^{max} \quad (3.32)$$

$\Delta\gamma$  and  $\Delta\tau$  are the strain range and shear stress range,  $\Delta\varepsilon_n$  and  $\Delta\sigma_n$  are the normal strain range and normal stress range, respectively.

## 4 Results and Discussion

### **The results of Dantas (2019):**

The following tables present the results of each fatigue test, including the loading mode, the normal and shear stress amplitudes, the stress R-ratio, and the number of cycles until specimen breakdown. The specimen was deemed exhausted, and the test was terminated after 5,000,000 cycles were completed without failure. All the specimens that were subjected to axial and multiaxial cyclic stress are shown in Figure 4.1 and 4.2. These findings demonstrate the influence of stress ratio, or more precisely, the effect of a mean stress, on fatigue life, as well as the extent to which a biaxial stress state may be more severe than a simple uniaxial stress state. Additionally, in the most recent biaxial testing, when shear stress was increased, the effect of this kind of stress on fatigue life was obvious. Additionally, the fracture surfaces of the specimens were viewed and analysed using an optical microscope to find certain changes between loading situations. As a result, Figures 4.3 – 4.6 illustrate the fracture behaviour and associated surfaces for each kind of force. When the origin of the crack is readily detected and is restricted to a single place, as is the case with specimens evaluated under axial loading (Figures 4.3 and 4.4) and proportional loading with a stress ratio near to 0, the origin of the fracture is indicated with an O, Figure 4.4. On the other hand, as seen in Figures 4.5 and 4.6, specimens subjected to totally reversed proportional loading exhibit various sources of fracture start, most likely owing to the shear stress effect. The fatigue and overload zones are easily distinguished in Figure 4.3 due to the significant increase in roughness between them. Additionally, a ratchet is denoted by the letter R, while in Figure 4.4, river markings indicate the direction of crack propagation and are denoted by the letter M.

Table 4.1 Result of uniaxial and multiaxial tests (Dantas, 2019)

| Loading Condition | Stress R-Ratio | $\sigma_a$ (MPa) | $\tau_a$ (MPa) | $\sigma_a / \tau_a$ | Nf (Cycles) |
|-------------------|----------------|------------------|----------------|---------------------|-------------|
| <b>Axial</b>      | 0.01           | 168              | -              | $\infty$            | $5 * 10^6$  |
|                   | 0.01           | 182              | -              | $\infty$            | $5 * 10^6$  |
|                   | 0.01           | 188              | -              | $\infty$            | $5 * 10^6$  |
|                   | 0.01           | 190              | -              | $\infty$            | $5 * 10^6$  |
|                   | 0.01           | 193              | -              | $\infty$            | $5 * 10^6$  |
|                   | 0.01           | 196              | -              | $\infty$            | 324373      |
|                   | 0.01           | 196              | -              | $\infty$            | 281589      |
|                   | 0.01           | 202              | -              | $\infty$            | 621182      |
|                   | 0.01           | 202              | -              | $\infty$            | 131064      |
|                   | 0.01           | 207              | -              | $\infty$            | 247161      |
|                   | 0.01           | 207              | -              | $\infty$            | 315639      |
|                   | 0.01           | 216              | -              | $\infty$            | 122047      |
|                   | 0.01           | 216              | -              | $\infty$            | 76082       |
|                   | -1             | 232              | -              | $\infty$            | $5 * 10^6$  |
|                   | -1             | 232              | -              | $\infty$            | 2147377     |
|                   | -1             | 249              | -              | $\infty$            | 561786      |
|                   | -1             | 249              | -              | $\infty$            | 406826      |
|                   | -1             | 272              | -              | $\infty$            | 157983      |
| -1                | 272            | -                | $\infty$       | 986262              |             |
| <b>Multiaxial</b> | 0.01           | 151              | 75             | 2                   | $5 * 10^6$  |
|                   | 0.01           | 160              | 79             | 2                   | $5 * 10^6$  |
|                   | 0.01           | 165              | 82             | 2                   | $5 * 10^6$  |
|                   | 0.01           | 168              | 84             | 2                   | 332151      |
|                   | 0.01           | 168              | 84             | 2                   | 256955      |
|                   | 0.01           | 174              | 87             | 2                   | 313815      |
|                   | 0.01           | 174              | 87             | 2                   | 656534      |
|                   | 0.01           | 174              | 87             | 2                   | 181536      |
|                   | -1             | 164              | 82             | 2                   | $5 * 10^6$  |
|                   | -1             | 181              | 90             | 2                   | $5 * 10^6$  |
|                   | -1             | 194              | 99             | 2                   | 2536156     |
|                   | -1             | 194              | 99             | 2                   | 2040566     |
|                   | -1             | 204              | 104            | 2                   | 133962      |
|                   | -1             | 204              | 104            | 2                   | 835602      |
|                   | -1             | 204              | 104            | 2                   | 390101      |
|                   | -1             | 204              | 104            | 2                   | 383422      |
|                   | -1             | 164              | 164            | 1                   | 88165       |
|                   | -1             | 164              | 164            | 1                   | 44152       |

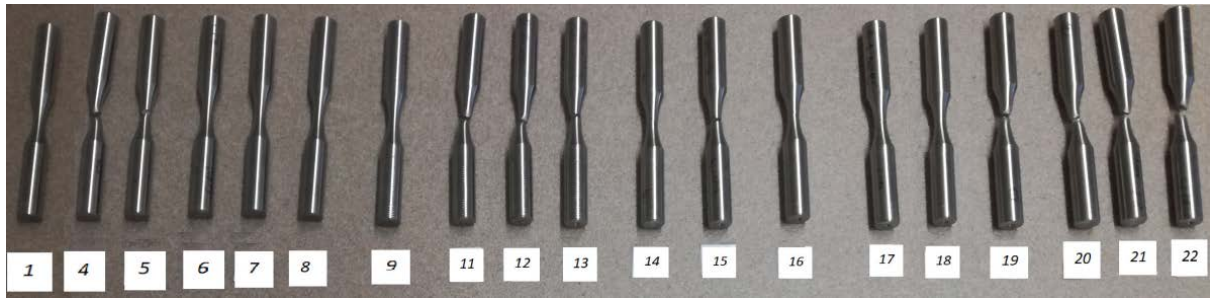


Figure 4.1 Specimens after axial fatigue tests (Dantas, 2019).

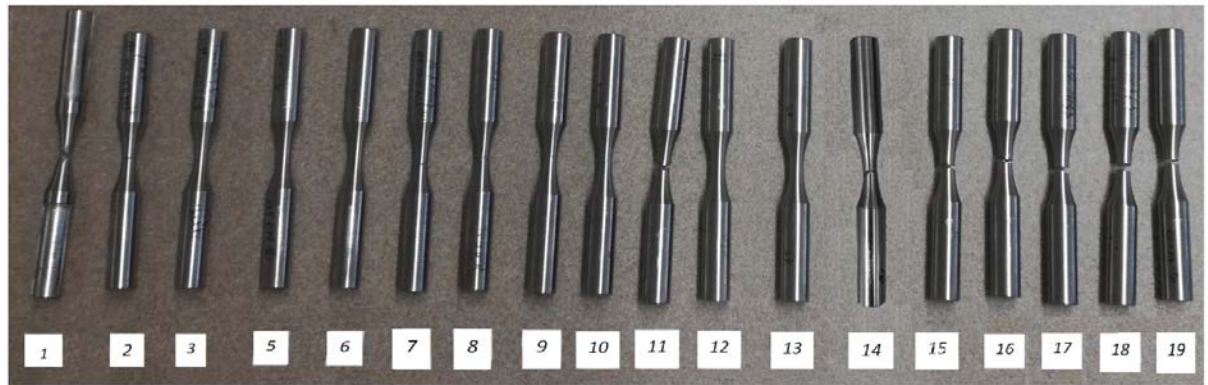


Figure 4.2 Specimens after multiaxial fatigue tests (Dantas, 2019).



Figure 4.3 Specimen tested under  $\sigma_a = 207$  MPa with  $R = 0.01$ . (Dantas, 2019)



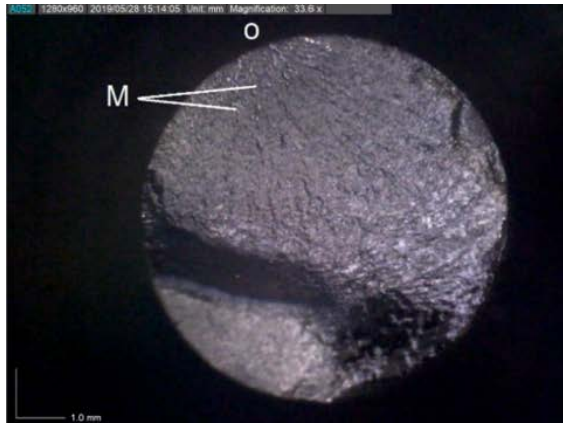


Figure 4.4 Specimen tested under  $\sigma_a = 272$  MPa with  $R = -1$  (Dantas, 2019).



Figure 4.5 Specimen tested under  $\sigma_a = 168$  MPa and  $\tau_a = 84$  MPa with  $R = 0.01$  (Dantas, 2019).



Figure 4.6 Specimen tested under  $\sigma_a = 204$  MPa and  $\tau_a = 104$  MPa with  $R = -1$  (Dantas, 2019)

**The results of Reis et al. (2006):**

Experiments were conducted using the sequence of loading pathways shown in Figure 4.7 to analyse the effects of multi-axial loading paths on fatigue crack paths. The testing of biaxial cyclic tension–compression and cyclic torsion was conducted using a biaxial servo-hydraulic Instron 8874 machine. The following were the test conditions: 4 –6 Hz in laboratory air at room temperature. The tests were concluded after the specimens were fully broken. Then, fractographic study of the macroscopic plane of fracture start and early crack development was performed using an optical microscope with 10 to 100 times magnification. Several broken specimens were also analysed using a SEM microscope. The orientation of the crack initiation plane was measured in the following way: first, the position of the crack initiation was found, as shown by the white arrow on the left side of Figures 4.8 and 4.9. Next, the specimen was measured in 3D, and the angle between the longitudinal axis and the crack initiation plane was found, as shown on the right side of Figures 4.8 and 4.9. This process and an example for each loading path are shown in Figures 4.8 and 4.9, respectively, for the two materials.

Several critical plane models and energy-based critical plane models, including the Findley, Brown–Miller, Fatemi–Socie, Smith–Watson-Topper, and Liu's criteria, are used to examine the possible orientation of the crack plane for the six biaxial loading instances shown in Figure 4.7.

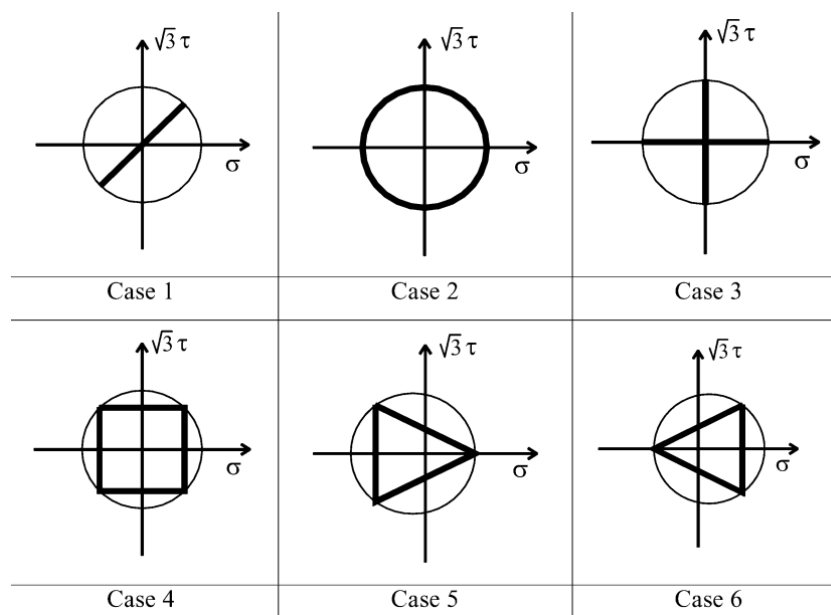


Figure 4.7 Multi-axial fatigue loading paths (Reis et al., 2006).

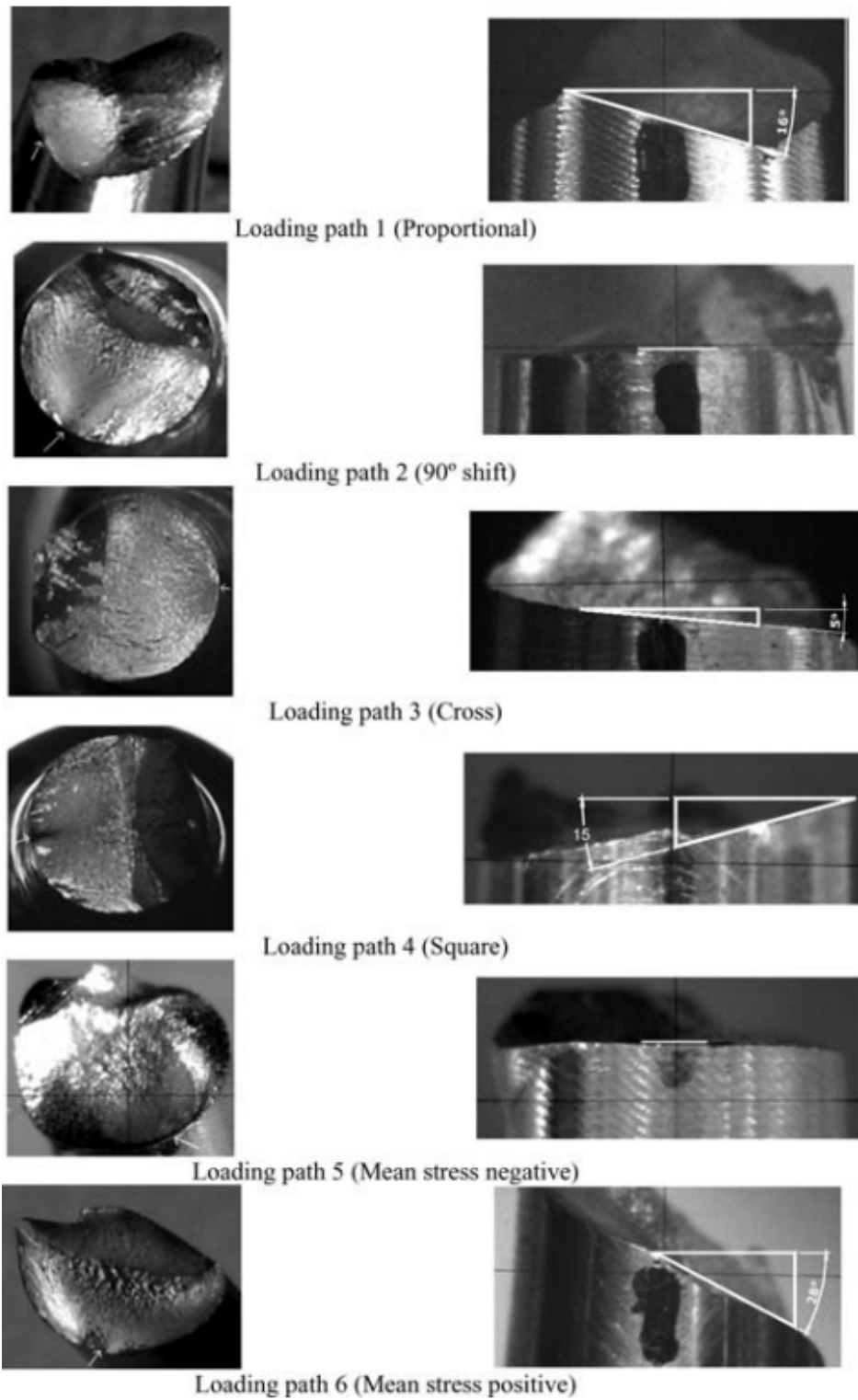


Figure 4.8 Fractographic analyses of the fatigue failure plane orientations under each of the six loading paths (42CrMo4) (Reis et al., 2006).

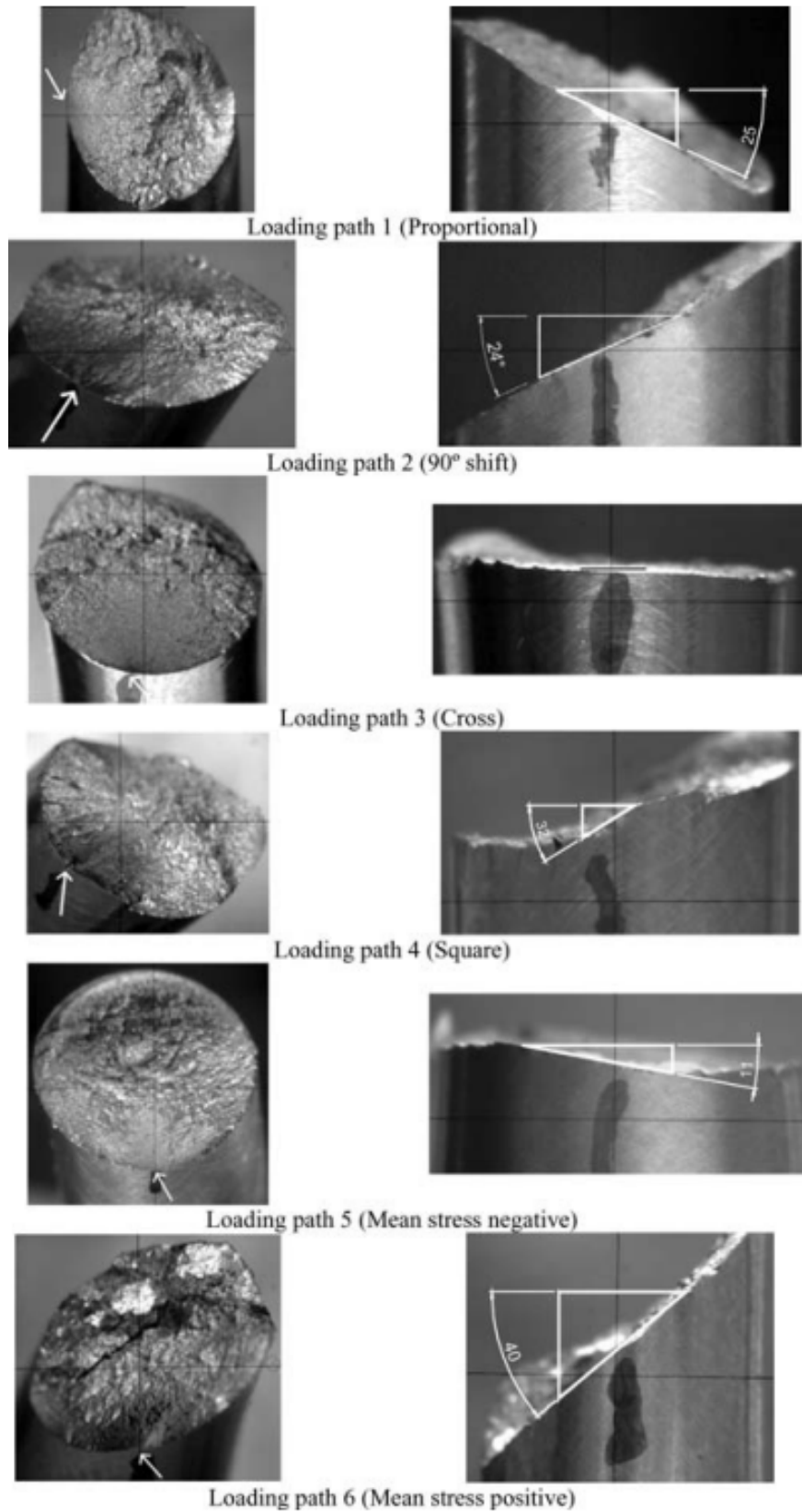


Figure 4.9 Fractographic analyses of the fatigue failure plane orientations under each of the six loading paths (AISI 303) (Reis et al., 2006).

In Table 4.2 for 42CrMo4 steel and Table 4.3 for AISI 303 stainless steel, the observed orientations of the early fracture propagation under different loading routes are shown. It is shown that loading pathways have a significant effect on crack orientations. From Case 1 through Case 6, the orientations of the cracks vary considerably. It is intriguing to notice that a significant number of nucleated fractures may be viewed under a microscope during the crack initiation stage, and that Ohkawa et al. (1997) reported comparable phenomena. As our test demonstrated, however, just a single major fracture developed during the early stages of propagation. In our investigation, Reis et al. (2006) thus solely considered this primary crack direction.

Table 4.2 Comparison of the observed crack plane with predictions for 42CrMo4 (Reis et al., 2006).

| <b>Multiaxial loading paths</b> |               |               |               |               |               |               |
|---------------------------------|---------------|---------------|---------------|---------------|---------------|---------------|
|                                 | <b>Case 1</b> | <b>Case 2</b> | <b>Case 3</b> | <b>Case 4</b> | <b>Case 5</b> | <b>Case 6</b> |
| <b>Crack plane observed</b>     | -16°          | 0°            | -5°           | 15°           | 0°            | -28°          |
| <b>Findley</b>                  | -16/65°       | 0°            | 0°            | ±21°          | 0°            | ±29°          |
| <b>Brown–Miller</b>             | -14/63°       | 0°            | 0°            | ±21°          | ±3°/<br>±27°  | ±27°/<br>±3°  |
| <b>Fatemi–Socie</b>             | -14/63°       | 0°            | 0°            | ±21°          | 0°            | ±29°          |
| <b>SWT</b>                      | 25°           | 0°            | 0°            | ±25°          | 0°            | ±25°          |
| <b>Liu I</b>                    | 25°           | 0°            | 0°            | ±25°          | ±15°          | ±15°          |
| <b>Liu II</b>                   | -21/69°       | 0°/±90°       | 0°/±90°       | ±21°/±69°     | 0°/±30°       | ±30°/0°       |

Table 4.3 Comparison of the observed crack plane with predictions for AISI 303 (Reis et al., 2006).

| <b>Multiaxial loading paths</b> |               |               |               |               |               |               |
|---------------------------------|---------------|---------------|---------------|---------------|---------------|---------------|
|                                 | <b>Case 1</b> | <b>Case 2</b> | <b>Case 3</b> | <b>Case 4</b> | <b>Case 5</b> | <b>Case 6</b> |
| <b>Crack plane observed</b>     | -25°          | 24°           | 0°            | 32°           | 0°            | 40°           |
| <b>Findley</b>                  | -15/63°       | 0°            | 0°            | ±22°          | 0°            | ±28°          |
| <b>Brown–Miller</b>             | -16/65°       | 0°            | 0°            | ±21°          | ±3°/±27°      | ±29°/±3°      |
| <b>Fatemi–Socie</b>             | -18/68°       | 0°            | 0°            | ±21°          | 0°            | ±29°          |
| <b>SWT</b>                      | 25°           | 0°            | 0°            | ±25°          | 0°            | ±25°          |
| <b>Liu I</b>                    | 25°           | 0°            | 0°            | ±25°          | ±15°          | ±15°          |
| <b>Liu II</b>                   | -21/69°       | 0°/±90°       | 0°/±90°       | ±21°/±69°     | 0°/±30°       | ±30°/0°       |

In the investigation of fatigue fracture pathways under multi-axial stress, many material-specific behaviours were discovered. If the material is brittle, as in Kim et al. (2004)'s 5% chrome work roll steel, the first phase of fracture propagation is characterised by extremely small crack diameters. As indicated by the test findings, the coefficient of extra strain hardening for AISI 303 stainless steel and 42CrMo4 steel is vastly different. The AISI 303 stainless steel coefficient is 0.90 and the 42CrMo4 steel coefficient is 0.18.

The AISI 303 stainless steel exhibits more extra cyclic hardening than the 42CrMo4 steel, and under identical loading patterns, different fracture orientations were detected for the two materials. Under loading case 2 (sinusoidal waveforms 90° out-of-phase), the observed crack orientation is 0° for the material 42CrMo4 and about 24° for the material AISI 303 stainless steel, which may be explained by the impact of further hardening. To validate the consistency of the observed fracture direction for loading case 2, many tests were conducted under loading case 2 at various loading levels, and the results are shown in Table 4.4. The average angle is shown to be 24.3°, while the standard deviation is merely 1.5. Also, for loading Case 4 (trapezoidal wave forms 90° out of phase), a

variation of 17° was recorded between AISI 303 and 42CrMo4. But for loading Case 1 (in-phase loading), when less far hardening is seen, a 9° divergence was detected between AISI 303 (-25°) and 42CrMo4 (-16°), most likely because of additional hardening (Reis et al., 2006).

Table 4.4 Loading vs measured crack plane results for AISI 303, loading Case 2 (Reis et al., 2006).

| $\Delta\sigma/2$ (MPa) | $\Delta\tau/2$ (MPa) | Angle (°) | Average angle (°) |
|------------------------|----------------------|-----------|-------------------|
| 300                    | 173.2                | 22.2      | 24.3              |
| 290                    | 167.4                | 25.3      |                   |
| 270                    | 155.9                | 23.6      |                   |
| 265                    | 153.0                | 24.1      |                   |

The degree of extra hardness seen in the 90° out-of-phase loading situation is dependent, from a metallurgical standpoint, on the ease with which numerous cross-slip systems arise in a particular material. Low stacking fault energy and widely spread dislocations are characteristics of AISI 303 stainless steel. During nonproportional loading, the planes of highest shear stress rotate, beginning plastic deformation along several slip systems. The fracture may have grown along one of the slip systems, including flaws, and as a result, its initial direction was diverse (Reis et al., 2006).

From a metallurgical perspective, the degree of extra hardness seen in the 90° out-of-phase loading situation depends on the ease with which numerous cross-slip systems form in a particular material (Socie & Marquis, 2000). The stacking fault energy and dislocation spacing in AISI 303 stainless steel are modest. During nonproportional loading, the planes of highest shear stress rotate, beginning plastic deformation along several slip systems. The fracture may have grown along one of the slip systems including flaws, as shown by the diverse direction of the first cracks (Reis et al., 2006).

**The results of Wu et al. (2014):**

The following tables (Table 4.5 and Table 4.6) summarises the experimental data, including axial and shear strain and stress amplitudes as well as failure life  $N_f$ .

Table 4.5 The experimental results for titanium alloy TC4 (Wu et al., 2014).

| <b>Phase angle (°)</b> | <b><math>\epsilon_a</math> (%)</b> | <b><math>\gamma_a</math> (%)</b> | <b><math>\sigma_a</math> (MPa)</b> | <b><math>\tau_a</math> (MPa)</b> | <b><math>N_f</math> (Cycles)</b> |
|------------------------|------------------------------------|----------------------------------|------------------------------------|----------------------------------|----------------------------------|
| -                      | 0.55                               | -                                | 610.2                              | -                                | 60048                            |
| -                      | 0.6                                | -                                | 655.2                              | -                                | 25069                            |
| -                      | 0.7                                | -                                | 728.6                              | -                                | 8457                             |
| -                      | 0.8                                | -                                | 738.9                              | -                                | 4135                             |
| -                      | 0.8                                | -                                | 766.4                              | -                                | 2544                             |
| -                      | 0.9                                | -                                | 772.5                              | -                                | 17083                            |
| -                      | 0.9                                | -                                | 746.4                              | -                                | 1730                             |
| -                      | 1.1                                | -                                | 755.2                              | -                                | 1007                             |
| -                      | 1.1                                | -                                | 746.7                              | -                                | 822                              |
| -                      | 1.3                                | -                                | 782.2                              | -                                | 510                              |
| -                      | 1.3                                | -                                | 787.6                              | -                                | 529                              |
| -                      | 1.5                                | -                                | 815.8                              | -                                | 339                              |
| -                      | 1.7                                | -                                | 819.2                              | -                                | 221                              |
| -                      | 2.0                                | -                                | 856.5                              | -                                | 124                              |
| -                      | 2.0                                | -                                | 861.6                              | -                                | 134                              |
| -                      | 2.3                                | -                                | 869.3                              | -                                | 89                               |
| -                      | 2.3                                | -                                | 861.7                              | -                                | 127                              |
| -                      | -                                  | 0.798                            | -                                  | 345.6                            | 69269                            |
| -                      | -                                  | 0.833                            | -                                  | 359.8                            | 51146                            |
| -                      | -                                  | 0.848                            | -                                  | 374.6                            | 37449                            |
| -                      | -                                  | 0.889                            | -                                  | 390.3                            | 17887                            |
| -                      | -                                  | 1.038                            | -                                  | 398.1                            | 7218                             |



Table 4.6 The experimental results for titanium alloy TC4 (Wu et al., 2014).

| <b>Phase angle (°)</b> | <b><math>\epsilon_a</math> (%)</b> | <b><math>\gamma_a</math> (%)</b> | <b><math>\sigma_a</math> (MPa)</b> | <b><math>\tau_a</math> (MPa)</b> | <b><math>N_f</math> (Cycles)</b> |
|------------------------|------------------------------------|----------------------------------|------------------------------------|----------------------------------|----------------------------------|
| -                      | -                                  | 1.302                            | -                                  | 431.2                            | 2691                             |
| -                      | -                                  | 1.645                            | -                                  | 417.8                            | 951                              |
| -                      | -                                  | 1.942                            | -                                  | 413.5                            | 459                              |
| -                      | -                                  | 2.309                            | -                                  | 404.5                            | 345                              |
| 0                      | 0.345                              | 0.648                            | 388.8                              | 278.5                            | 47195                            |
| 0                      | 0.427                              | 0.710                            | 466.4                              | 296.8                            | 20611                            |
| 0                      | 0.576                              | 0.938                            | 490.6                              | 292.8                            | 4141                             |
| 0                      | 0.687                              | 1.111                            | 532.1                              | 312.7                            | 1795                             |
| 0                      | 0.863                              | 1.371                            | 538.8                              | 299.4                            | 868                              |
| 0                      | 1.391                              | 2.038                            | 530.5                              | 261                              | 351                              |
| 45                     | 0.391                              | 0.643                            | 435.6                              | 276.9                            | 20953                            |
| 45                     | 0.418                              | 0.702                            | 472                                | 303.2                            | 9478                             |
| 45                     | 0.496                              | 0.831                            | 545.2                              | 342.6                            | 4798                             |
| 45                     | 0.620                              | 1.043                            | 592                                | 340.9                            | 1563                             |
| 45                     | 0.772                              | 1.255                            | 629                                | 341.3                            | 683                              |
| 45                     | 1.224                              | 1.756                            | 679.8                              | 353.8                            | 185                              |
| 90                     | 0.349                              | 0.639                            | 392.8                              | 279.6                            | 45138                            |
| 90                     | 0.418                              | 0.704                            | 475.7                              | 307.8                            | 37273                            |
| 90                     | 0.499                              | 0.821                            | 562.6                              | 356.4                            | 11152                            |
| 90                     | 0.556                              | 0.934                            | 623.6                              | 401.2                            | 2332                             |
| 90                     | 0.632                              | 1.079                            | 703.2                              | 427.7                            | 1017                             |
| 90                     | 1.229                              | 1.700                            | 678.6                              | 382.3                            | 233                              |

On titanium alloy TC4 specimens, multiaxial fatigue tests as well as uniaxial and pure torsional testing were done. Based on the test results, six multiaxial fatigue prediction models were assessed. The key findings are as follows:

Under 45o and 90o out-of-phase loading conditions, increased hardening of titanium alloy TC4 was found. Nonproportional loading routes have no effect on fatigue damage in

short-life regions. Effective strain, maximum shear strain, and the Smith–Watson–Topper criterion tend to provide nonconservative findings. The shear strain-based critical plane techniques (Kandil, Brown, and Miller parameter and Fatemi and Socie parameter) have comparable life prediction capabilities. The prediction results based on these two parameters are almost within a two-factor scatter band of the test findings, except for a few data points in the long-life area. Because extra hardening has less of an impact on fatigue damage in the area of long life, the benefit that Fatemi and Socie parameters can explain for increased hardening in titanium alloy TC4 is not shown (Wu et al., 2014).

### **The results of Kallmeyer et al. (2002):**

In addition to the biaxial data, more than 100 points of uniaxial fatigue data were collected and evaluated. As part of a round-robin programme done by the U.S. Air Force and numerous turbine engine manufacturers to address the issue of high cycle fatigue HCF failures in gas turbine engines, uniaxial tests were conducted on the same material. The uniaxial experiments referenced in this article were done at room temperature under both strain-controlled and load-controlled circumstances and throughout a variety of stress ratios, including  $R = -0.1$ ,  $R = 0.5$ , and  $R = -0.1$  as short life testing. Test frequencies varied from 0.33 Hz strain-controlled to 1000 Hz load-controlled as long-life tests. Even though these frequencies are quite high, tests revealed that specimen heating was negligible. Moreover, this program's statistics imply that the fatigue life of Ti-6Al-4V does not vary much in frequency within the studied range (Kallmeyer et al., 2002).

The uniaxial fatigue data is shown in Figure 4.10. Within the area of data overlap, there is a relatively smooth transition between strain-controlled and stress-controlled data, showing largely linear elastic behaviour. The agreement of data in the overlap zone further suggests that fracture nucleation rather than lengthy crack development predominates in this area. Notably, there is a considerable gap in the results across the tested stress ratios, especially for longer fatigue durations. Clearly, the existence of a tensile mean stress modifies the permissible stress amplitude for Ti-6Al-4V considerably. The completely reversed uniaxial data served as a reference point for comparing the multiaxial fatigue models and evaluating their capabilities when mean stresses arise.

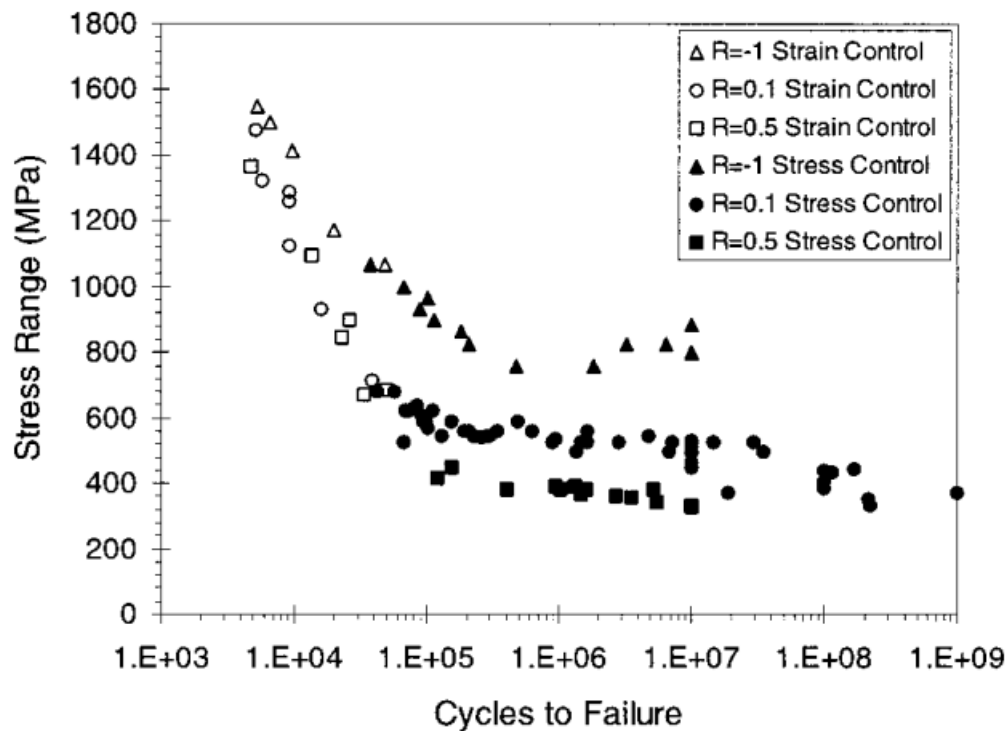


Figure 4.10 Uniaxial fatigue data (Kallmeyer et al., 2002).

The biaxial fatigue data collected by this research is reported in Table 4.7, organised by test type. The first series of tests in the table (21-11 to 21-4) consists of torsion-only experiments conducted at varying stress ratios. These studies were conducted to determine whether or not average shear loads affect fatigue lifetimes. Investigations at loading levels near to the endurance limit for low carbon steels led to the widespread notion that torsional mean stresses do not affect fatigue life. However, when the highest shear stress surpasses about 80% of the torsional yield strength, the allowed stress amplitude in bending or torsion is decreased compared to the completely reversed situation. A static or mean shear stress has little effect on metal fatigue strength when the maximum stress is less than 80% of the torsional yield strength. Torsion experiments were done at stress ratios ( $\tau_{\min}/\tau_{\max}$ ) of  $R = -1, 0.1,$  and  $0.5$  in order to assess the impact of mean shear stresses on the fatigue behaviour of Ti-6Al-4V (Kallmeyer et al., 2002).

Table 4.7 The experimental results Ti-6Al-4V (Kallmeyer et al., 2002).

| <b>Spec. ID</b> | $\epsilon_{max}$<br>% | $\epsilon_{min}$<br>% | $\gamma_{max}$<br>% | $\gamma_{min}$<br>% | $\sigma_{max}$<br>MPa | $\sigma_{min}$<br>MPa | $\tau_{max}$<br>MPa | $\tau_{min}$<br>MPa | $N_f$<br>Cycles | <b>Test Cond.</b> |
|-----------------|-----------------------|-----------------------|---------------------|---------------------|-----------------------|-----------------------|---------------------|---------------------|-----------------|-------------------|
| <b>21-11</b>    | -                     | -                     | 0.866               | -0.86               | 0                     | 0                     | 375.8               | -375.5              | 72141           | Torsion<br>R=-1   |
| <b>21-6</b>     | -                     | -                     | 0.614               | -0.61               | 0                     | 0                     | 266.2               | -264.7              | 241250          | Torsion<br>R=-1   |
| <b>156-10</b>   | -                     | -                     | 0.56                | -0.56               | 0                     | 0                     | 242.7               | -244.1              | 961806          | Torsion<br>R=-1   |
| <b>21-7</b>     | -                     | -                     | 1.81                | 0.166               | 0                     | 0                     | 454                 | -252                | 30007           | Torsion<br>R=0.1  |
| <b>156-5</b>    | -                     | -                     | 1.21                | 0.09                | 0                     | 0                     | 433                 | -38.6               | 150293          | Torsion<br>R=0.1  |
| <b>156-4</b>    | -                     | -                     | 1.36                | 0.150               | 0                     | 0                     | 448                 | -71.7               | 151598          | Torsion<br>R=0.1  |
| <b>156-1</b>    | -                     | -                     | 0.96                | 0.086               | 0                     | 0                     | 415.7               | 47.2                | 814753          | Torsion<br>R=0.1  |
| <b>21-4</b>     | -                     | -                     | 1.96                | 0.815               | 0                     | 0                     | 455.7               | -36.5               | 141229          | Torsion<br>R=0.5  |
| <b>21-1</b>     | 0.31                  | -0.31                 | 0.416               | -0.42               | 365.4                 | -365.4                | 180.6               | -181.3              | 67965           | Prop.<br>R= -1    |
| <b>156-9</b>    | 0.462                 | 0.049                 | 0.616               | 0.055               | 540.6                 | 57.2                  | 267                 | 24.1                | 60514           | Prop.<br>R= 0.1   |
| <b>156-3</b>    | 0.464                 | 0.048                 | 0.621               | 0.055               | 543                   | 55.8                  | 269                 | 24.1                | 87920           | Prop.<br>R= 0.1   |
| <b>156-8</b>    | 0.303                 | -0.30                 | 0.406               | -0.41               | 352.5                 | -350.9                | 175.2               | -176.5              | 111783          | 90°<br>R=-1       |
| <b>156-2</b>    | 0.362                 | -0.37                 | 0.471               | -0.47               | 424                   | -436                  | 204                 | -204                | 38355           | Triangle<br>path  |
| <b>21-2</b>     | 0.364                 | -0.37                 | 0.471               | -0.47               | 4261                  | -435.8                | 204.1               | -206.8              | 43009           | Triangle<br>path  |
| <b>21-9</b>     | 0.364                 | -0.36                 | 0.475               | 0.004               | 426                   | -426                  | 206.2               | 2.1                 | 71358           | Z leg             |
| <b>21-5</b>     | 0.365                 | -0.36                 | 0.005               | -0.47               | 427.5                 | -424.7                | -2.1                | -206.2              | 79367           | X leg             |
| <b>21-8</b>     | 0.091                 | 0.09                  | 0.66                | -0.66               | 106.2                 | 104.8                 | 288.9               | -288.2              | 72124           | Y+ leg            |

|              |       |       |      |       |        |        |       |        |        |        |
|--------------|-------|-------|------|-------|--------|--------|-------|--------|--------|--------|
| <b>21-3</b>  | 0.090 | 0.09  | 0.66 | -0.66 | 105.5  | 104.1  | 288.9 | -288.9 | 73728  | Y+ leg |
| <b>21-10</b> | -0.09 | -0.09 | 0.66 | -0.66 | -104.1 | -106.9 | 288.9 | -288.9 | 329058 | Y- leg |

The next three tests (21-1 to 156-3) include proportionate, coupled axial torsion. The purpose of these tests was to assess the combined mean stress performance of the damage parameters, where the torsional mean stresses were deemed destructive based on the prior series of studies. The subsequent tests are nonproportional and contain multidimensional mean stresses in certain instances. Specimen 156-8 was loaded with a 90-degree sinusoidal lag between the shear and axial strain Figure 4.11a, as shown. This load route is often regarded as crucial in terms of deformation and fatigue damage. The remainder of the nonproportional tests were loaded along a triangular route Figure. 4.11b, which approximates out-of-phase service circumstances. The specimens 156-2 and 21-2 were loaded along the whole triangle route, while the other specimens (21-9 to 21-10) were loaded along parts of this path (X, Y, or Z), as shown in Figure 2b. The -Y and +Y notations indicate whether the static axial strain was positive or negative in these tests with just cyclic torsional stresses. Additionally, two experiments were done on the diagonal sides (X and Z) of the triangle (Kallmeyer et al., 2002).

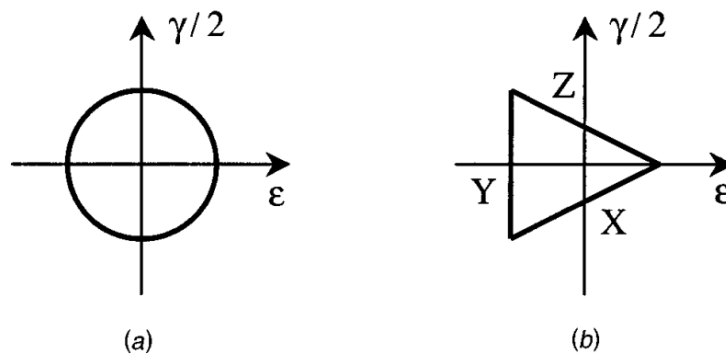


Figure 4.11 Nonproportional strain paths: (a) 90° out of phase (O-P) path and (b) triangle path (Kallmeyer et al., 2002).

**The results of Yang et al. (2022):**

Estimated SM45C results:

Based on the SM45C test data in Table 4.8, Figure 4.12 depicts the expected results from the suggested multi-axial and high-cycle fatigue failure model. As seen in Figure 4.12a, the projected values for the uniaxial tension/compression condition are within 2 times the scatter range of fatigue life. Under pure torsional stress, the anticipated results are generally within  $\pm 2$  times the scatter band of fatigue life, with the exception of individual prediction values, which are within  $\pm 3$  times the scatter band. In the case of proportionate tension-torsion loading, as seen in Figure 4.12b, the conservative forecast result is about three times the scatter band of fatigue life. In the event of a phase difference of 90, the majority of forecast results fall within the  $\pm 2$ -time scatter band of fatigue life, but a few are close to the 3-time scatter band (Yang et al., 2022).

Table 4.8 Test data of SM45C (Yang et al., 2022)

| $\sigma_{xy,a}$ (MPa) | $\sigma_{xy,m}$ (MPa) | $\tau_{xy,a}$ (MPa) | $\tau_{xy,m}$ (MPa) | Phase (°) | $N_f$ (Cycles) |
|-----------------------|-----------------------|---------------------|---------------------|-----------|----------------|
| 413.4                 | 0                     | 0                   | 0                   | 0         | 14921          |
| 389.1                 | 0                     | 0                   | 0                   | 0         | 25972          |
| 373.5                 | 0                     | 0                   | 0                   | 0         | 52288          |
| 366.8                 | 0                     | 0                   | 0                   | 0         | 73480          |
| 354.1                 | 0                     | 0                   | 0                   | 0         | 91209          |
| 337.3                 | 0                     | 0                   | 0                   | 0         | 101076         |
| 324.1                 | 0                     | 0                   | 0                   | 0         | 163940         |
| 314.9                 | 0                     | 0                   | 0                   | 0         | 210131         |
| 313                   | 0                     | 0                   | 0                   | 0         | 323068         |
| 295.2                 | 0                     | 0                   | 0                   | 0         | 446301         |
| 294.2                 | 0                     | 0                   | 0                   | 0         | 714643         |
| 0                     | 0                     | 280.4               | 0                   | 0         | 10370          |
| 0                     | 0                     | 257.7               | 0                   | 0         | 19918          |
| 0                     | 0                     | 279.2               | 0                   | 0         | 23486          |
| 0                     | 0                     | 256.8               | 0                   | 0         | 30169          |
| 0                     | 0                     | 249.5               | 0                   | 0         | 108937         |

|     |   |       |   |    |         |
|-----|---|-------|---|----|---------|
| 0   | 0 | 231.1 | 0 | 0  | 140230  |
| 0   | 0 | 247.7 | 0 | 0  | 163940  |
| 0   | 0 | 233.1 | 0 | 0  | 322893  |
| 0   | 0 | 227.9 | 0 | 0  | 42734   |
| 0   | 0 | 220.4 | 0 | 0  | 1127312 |
| 390 | 0 | 151   | 0 | 0  | 8500    |
| 349 | 0 | 148   | 0 | 0  | 24000   |
| 325 | 0 | 153   | 0 | 0  | 32000   |
| 372 | 0 | 93    | 0 | 0  | 38000   |
| 309 | 0 | 134   | 0 | 0  | 100000  |
| 265 | 0 | 225   | 0 | 90 | 12000   |
| 392 | 0 | 118   | 0 | 90 | 12400   |
| 417 | 0 | 78    | 0 | 90 | 13000   |
| 346 | 0 | 173   | 0 | 90 | 16000   |
| 245 | 0 | 216   | 0 | 90 | 20000   |
| 304 | 0 | 185   | 0 | 90 | 26000   |
| 304 | 0 | 152   | 0 | 90 | 57000   |
| 314 | 0 | 127   | 0 | 90 | 100000  |
| 286 | 0 | 143   | 0 | 90 | 120000  |
| 167 | 0 | 211   | 0 | 90 | 29000   |
| 265 | 0 | 132   | 0 | 90 | 350000  |

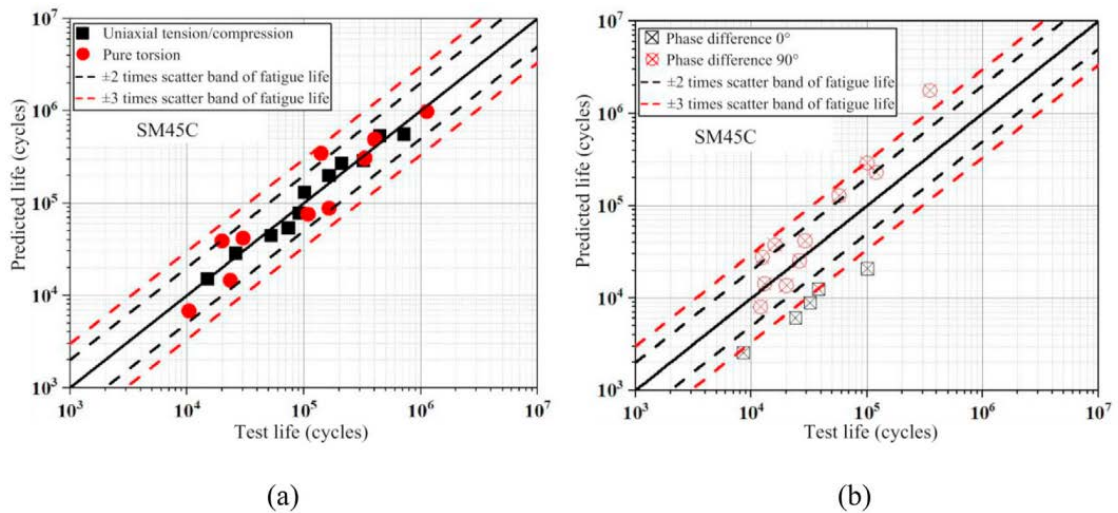


Figure 4.12 Prediction of the service life of SM45C under (a) uniaxial tension/compression loading and pure torsion loading and (b) tension/torsion loading (Yang et al., 2022).

Estimated SAE1045 results:

Based on the test data of SAE1045 under tension and torsion loads shown in Table 4.9, Figure 4.13 depicts the expected outcomes of the suggested multi-axial and high-cycle fatigue failure models. As seen in Figure 4.13a, for the uniaxial tension/compression and pure torsion cases, the predicted fatigue life is close to the experimental fatigue life. As seen in Figure 4.13b, the prediction findings for the tension-torsion loading example are quite conservative. A handful of the projections are close to  $\pm 3$  times the scatter band of fatigue life, while the majority are within  $\pm 2$  times the scatter band (Yang et al., 2022).

Table 4.9 Test data of SAE 1045 tension-torsion loading (Yang et al., 2022).

| $\sigma_{xy,a}$<br>(MPa) | $\sigma_{xy,m}$<br>(MPa) | $\tau_{xy,a}$<br>(MPa) | $\tau_{xy,m}$<br>(MPa) | Phase<br>(°) | $N_f$<br>(Cycles) |
|--------------------------|--------------------------|------------------------|------------------------|--------------|-------------------|
| 177.4                    | 0                        | 0                      | 0                      | 0            | 1084              |
| 177.4                    | 0                        | 0                      | 0                      | 0            | 1423              |
| 177.4                    | 0                        | 0                      | 0                      | 0            | 1444              |
| 162.6                    | 0                        | 0                      | 0                      | 0            | 1859              |



|       |   |       |   |   |       |
|-------|---|-------|---|---|-------|
| 162.6 | 0 | 0     | 0 | 0 | 2186  |
| 1626  | 0 | 0     | 0 | 0 | 2178  |
| 147.8 | 0 | 0     | 0 | 0 | 4282  |
| 147.8 | 0 | 0     | 0 | 0 | 4134  |
| 147.8 | 0 | 0     | 0 | 0 | 4699  |
| 133   | 0 | 0     | 0 | 0 | 10643 |
| 133   | 0 | 0     | 0 | 0 | 8785  |
| 133   | 0 | 0     | 0 | 0 | 9776  |
| 0     | 0 | 136.5 | 0 | 0 | 847   |
| 0     | 0 | 136.5 | 0 | 0 | 1104  |
| 0     | 0 | 136.5 | 0 | 0 | 915   |
| 0     | 0 | 125.1 | 0 | 0 | 2034  |
| 0     | 0 | 125.1 | 0 | 0 | 2306  |
| 0     | 0 | 125.1 | 0 | 0 | 2961  |
| 0     | 0 | 113.7 | 0 | 0 | 4934  |
| 0     | 0 | 113.7 | 0 | 0 | 4373  |
| 0     | 0 | 113.7 | 0 | 0 | 3141  |
| 0     | 0 | 102.3 | 0 | 0 | 9205  |
| 0     | 0 | 102.3 | 0 | 0 | 9611  |
| 0     | 0 | 102.3 | 0 | 0 | 9797  |
| 148.5 | 0 | 74.3  | 0 | 0 | 1121  |
| 148.5 | 0 | 74.3  | 0 | 0 | 1014  |
| 148.5 | 0 | 74.3  | 0 | 0 | 1196  |
| 127.3 | 0 | 63.7  | 0 | 0 | 3577  |
| 127.3 | 0 | 63.7  | 0 | 0 | 379   |
| 127.3 | 0 | 63.7  | 0 | 0 | 3602  |
| 120.2 | 0 | 60.1  | 0 | 0 | 5400  |
| 120.2 | 0 | 60.1  | 0 | 0 | 5131  |
| 120.2 | 0 | 60.1  | 0 | 0 | 4291  |
| 113.2 | 0 | 58.6  | 0 | 0 | 8039  |
| 113.2 | 0 | 58.6  | 0 | 0 | 9193  |
| 113.2 | 0 | 58.6  | 0 | 0 | 8500  |

|      |   |       |   |   |       |
|------|---|-------|---|---|-------|
| 58.2 | 0 | 116.4 | 0 | 0 | 1830  |
| 58.2 | 0 | 116.4 | 0 | 0 | 1556  |
| 58.2 | 0 | 116.4 | 0 | 0 | 1702  |
| 53.4 | 0 | 106.7 | 0 | 0 | 3768  |
| 53.4 | 0 | 106.7 | 0 | 0 | 3684  |
| 53.4 | 0 | 106.7 | 0 | 0 | 3176  |
| 48.5 | 0 | 97    | 0 | 0 | 6717  |
| 48.5 | 0 | 97    | 0 | 0 | 6054  |
| 48.5 | 0 | 97    | 0 | 0 | 5097  |
| 43.7 | 0 | 87.3  | 0 | 0 | 12531 |
| 43.7 | 0 | 87.3  | 0 | 0 | 17340 |
| 43.7 | 0 | 87.3  | 0 | 0 | 15382 |

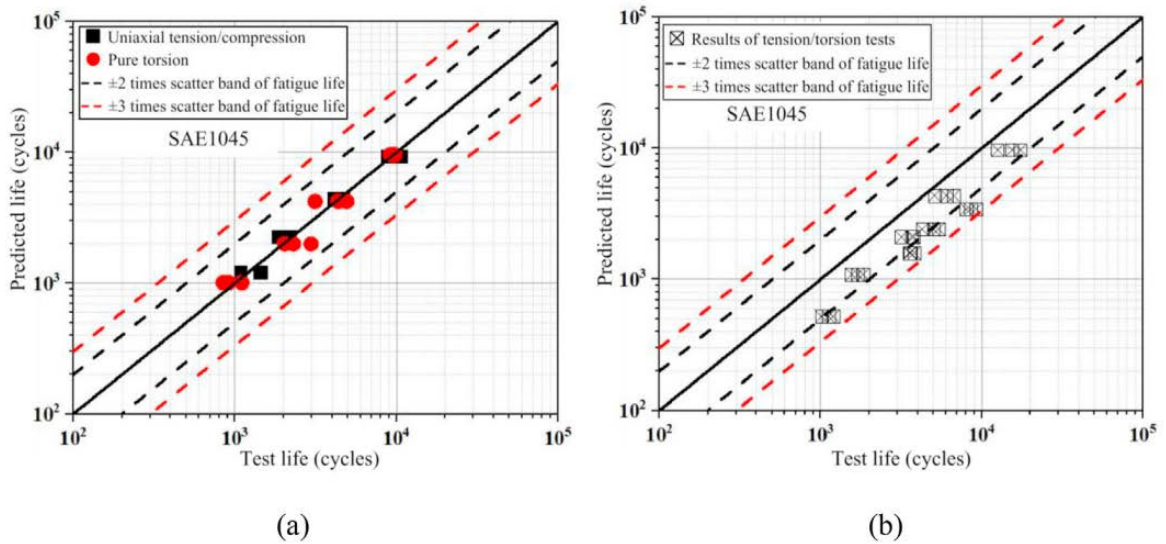


Figure 4.13 Prediction of the service life of SAE1045 under (a) the uniaxial tension/compression loading and the pure torsion loading and (b) the tension-torsion loading (Yang et al., 2022).

Figure 4.14 depicts the prediction results of the proposed multi-axial and high-cycle fatigue failure models based on the test data of SAE1045 under bending and torsion loads found in Table 4.10. As demonstrated in Figure 4.14a, the projected values for uniaxial tension/compression and pure torsion instances are within  $\pm 2$  times the scatter band of fatigue life. Figure 4.14b depicts the findings of the bending torsion loading scenario. The

majority of the anticipated values for proportional loading with phase difference  $0^\circ$  is within 2 times the scatter band of fatigue life, while some are within 3 times the scatter band of fatigue life. Most of the prediction findings for the non-proportional loading scenario with a phase difference of  $90^\circ$  are within the  $\pm 2$ -time scatter range of fatigue life, while individual data points are close to the  $\pm 3$ -time scatter band of fatigue life (Yang et al., 2022).

Table 4.10 Test data of SAE 1045 bending-torsion loading (Yang et al., 2022)

| $\sigma_{xy,a}$<br>(MPa) | $\sigma_{xy,m}$<br>(MPa) | $\tau_{xy,a}$<br>(MPa) | $\tau_{xy,m}$<br>(MPa) | Phase<br>( $^\circ$ ) | $N_f$<br>(Cycles) |
|--------------------------|--------------------------|------------------------|------------------------|-----------------------|-------------------|
| 445.6                    | 0                        | 0                      | 0                      | 0                     | 8262              |
| 413.8                    | 0                        | 0                      | 0                      | 0                     | 13060             |
| 413.8                    | 0                        | 0                      | 0                      | 0                     | 13760             |
| 413.8                    | 0                        | 0                      | 0                      | 0                     | 18310             |
| 411.6                    | 0                        | 0                      | 0                      | 0                     | 17450             |
| 298.4                    | 0                        | 0                      | 0                      | 0                     | 106700            |
| 298.4                    | 0                        | 0                      | 0                      | 0                     | 117700            |
| 275.3                    | 0                        | 0                      | 0                      | 0                     | 83600             |
| 275.3                    | 0                        | 0                      | 0                      | 0                     | 184300            |
| 275.3                    | 0                        | 0                      | 0                      | 0                     | 132300            |
| 275.3                    | 0                        | 0                      | 0                      | 0                     | 228300            |
| 271.8                    | 0                        | 0                      | 0                      | 0                     | 249900            |
| 234.8                    | 0                        | 0                      | 0                      | 0                     | 403800            |
| 234.8                    | 0                        | 0                      | 0                      | 0                     | 709000            |
| 232.4                    | 0                        | 0                      | 0                      | 0                     | 764000            |
| 0                        | 0                        | 159.2                  | 0                      | 0                     | 1293000           |
| 0                        | 0                        | 159.2                  | 0                      | 0                     | 2238000           |
| 0                        | 0                        | 259.2                  | 0                      | 0                     | 2000000           |
| 0                        | 0                        | 191                    | 0                      | 0                     | 101100            |
| 0                        | 0                        | 191                    | 0                      | 0                     | 164070            |
| 0                        | 0                        | 238.7                  | 0                      | 0                     | 9528              |

|       |   |       |   |   |         |
|-------|---|-------|---|---|---------|
| 0     | 0 | 238.7 | 0 | 0 | 14720   |
| 90.7  | 0 | 201.6 | 0 | 0 | 33330   |
| 90.7  | 0 | 173.5 | 0 | 0 | 177800  |
| 90.7  | 0 | 173.5 | 0 | 0 | 186700  |
| 124.1 | 0 | 173.5 | 0 | 0 | 142700  |
| 124.1 | 0 | 173.5 | 0 | 0 | 169500  |
| 133.7 | 0 | 214.9 | 0 | 0 | 24540   |
| 134.5 | 0 | 143.2 | 0 | 0 | 396800  |
| 135.4 | 0 | 214.9 | 0 | 0 | 17730   |
| 157.6 | 0 | 110.6 | 0 | 0 | 587000  |
| 157.6 | 0 | 110.6 | 0 | 0 | 1194000 |
| 183   | 0 | 214.9 | 0 | 0 | 12700   |
| 194.2 | 0 | 135.3 | 0 | 0 | 124500  |
| 194.2 | 0 | 136.1 | 0 | 0 | 163700  |
| 194.2 | 0 | 136.1 | 0 | 0 | 158100  |
| 198.9 | 0 | 70    | 0 | 0 | 722500  |
| 198.9 | 0 | 70    | 0 | 0 | 747000  |
| 198.9 | 0 | 214.9 | 0 | 0 | 10420   |
| 206.9 | 0 | 111.4 | 0 | 0 | 226000  |
| 215.7 | 0 | 202.9 | 0 | 0 | 11630   |
| 246.7 | 0 | 86.7  | 0 | 0 | 159900  |
| 246.7 | 0 | 86.7  | 0 | 0 | 220500  |
| 267.4 | 0 | 71.6  | 0 | 0 | 153800  |
| 267.4 | 0 | 76.4  | 0 | 0 | 65049   |
| 273.7 | 0 | 107.4 | 0 | 0 | 51780   |
| 273.7 | 0 | 107.4 | 0 | 0 | 65800   |
| 294.4 | 0 | 167.1 | 0 | 0 | 11500   |
| 294.4 | 0 | 167.1 | 0 | 0 | 11630   |
| 294.4 | 0 | 202.9 | 0 | 0 | 5113    |
| 318.3 | 0 | 167.1 | 0 | 0 | 12050   |
| 370   | 0 | 107.4 | 0 | 0 | 11380   |
| 370   | 0 | 107.4 | 0 | 0 | 12090   |

|       |   |       |   |    |        |
|-------|---|-------|---|----|--------|
| 183   | 0 | 214.9 | 0 | 90 | 13110  |
| 294.4 | 0 | 167.1 | 0 | 90 | 27470  |
| 286.5 | 0 | 167.1 | 0 | 90 | 24620  |
| 270.2 | 0 | 178.4 | 0 | 90 | 10840  |
| 366.1 | 0 | 105.4 | 0 | 90 | 23980  |
| 122.5 | 0 | 173.5 | 0 | 90 | 157100 |
| 206.1 | 0 | 136.1 | 0 | 90 | 45580  |
| 194.2 | 0 | 136.1 | 0 | 90 | 213800 |
| 194.2 | 0 | 136.1 | 0 | 90 | 266200 |

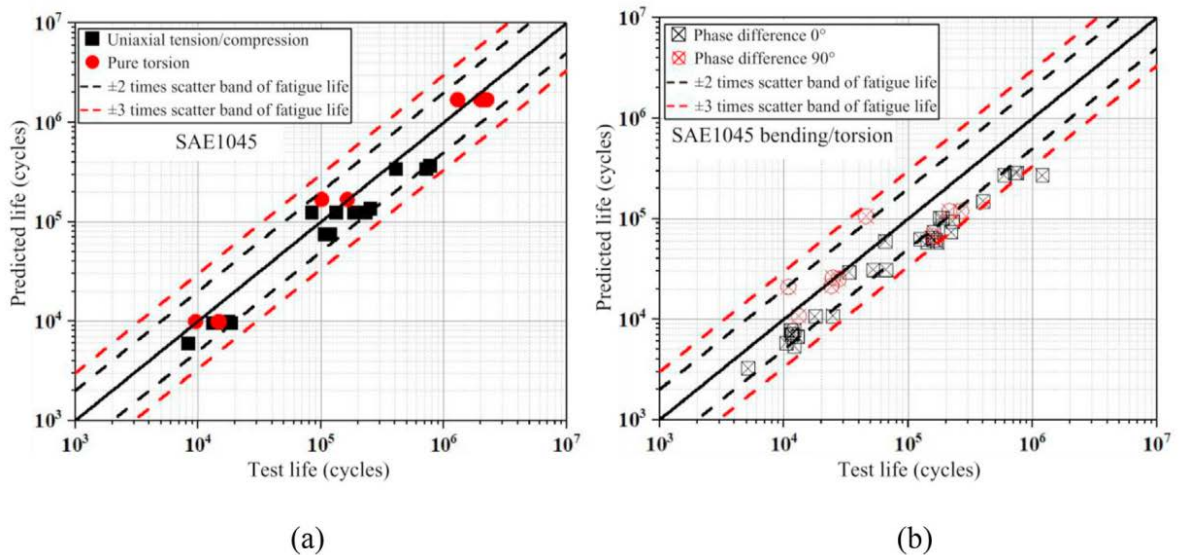


Figure 4.14 SAE1045 life prediction under (a) uniaxial tension/compression and pure torsion loads and (b) bending-torsion loads (Yang et al., 2022).

Estimated LY12CZ results:

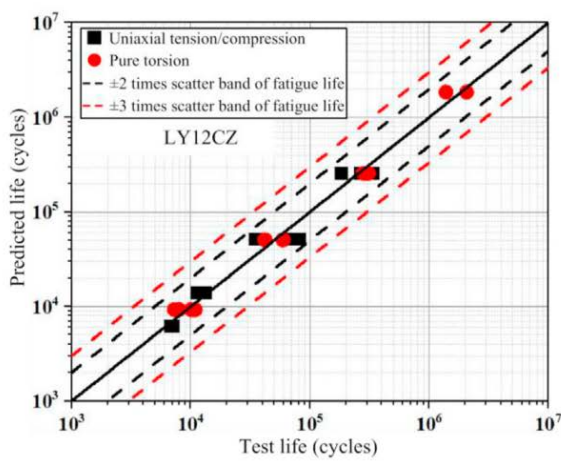
Based on the test data of LY12CZ under tension/torsion loads presented in Table 4.11, the suggested multi-axial and high-cycle fatigue failure models' prediction findings are shown in Figure 4.15. For uniaxial tension/compression and pure torsion instances, as illustrated in Fig. 4.15a, the predicted fatigue life is in close proximity to the experimental fatigue life. Figure 4.15b displays the results of tension-torsion loading. For the phase differences of  $0^\circ$ ,  $30^\circ$ , and  $45^\circ$ , the majority of anticipated outcomes fall within  $\pm 2$  times the scatter band of fatigue life, whereas only a few values fall within 3 times the scatter

band. Although the forecast results for the phase difference between 60° and 90° are scattered, the majority of the values fall within  $\pm 3$  times the scatter band of fatigue life. Some of the predicted outcomes for the phase difference are greater than the experimental ones. This is since the equivalent stress in some tests is rather high, which is close to the range of low-cycle fatigue (Yang et al., 2022).

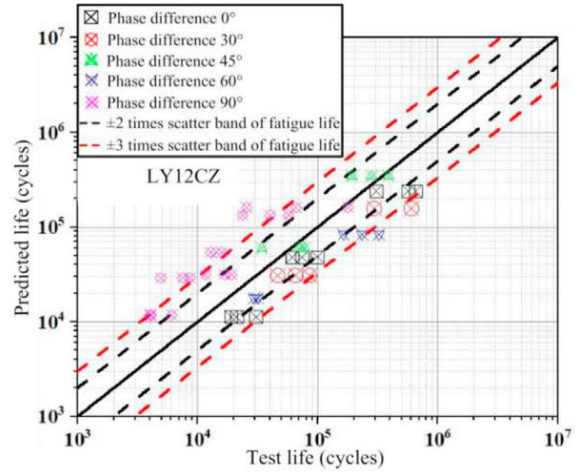
Table 4.11 Test data of LY12CZ (Yang et al., 2022).

| $\sigma_{xy,a}$<br>(MPa) | $\sigma_{xy,m}$<br>(MPa) | $\tau_{xy,a}$<br>(MPa) | $\tau_{xy,m}$<br>(MPa) | Phase<br>(°) | $N_f$<br>(Cycles) |
|--------------------------|--------------------------|------------------------|------------------------|--------------|-------------------|
| 158.1                    | 0                        | 111.8                  | 0                      | 0            | 99385             |
| 158.1                    | 0                        | 111.8                  | 0                      | 0            | 61203             |
| 158.1                    | 0                        | 111.8                  | 0                      | 0            | 73463             |
| 126.5                    | 0                        | 91.6                   | 0                      | 0            | 562025            |
| 126.5                    | 0                        | 91.6                   | 0                      | 0            | 651726            |
| 126.5                    | 0                        | 91.6                   | 0                      | 0            | 306988            |
| 189.7                    | 0                        | 137.4                  | 0                      | 0            | 30589             |
| 189.7                    | 0                        | 137.4                  | 0                      | 0            | 21034             |
| 189.7                    | 0                        | 137.4                  | 0                      | 0            | 18919             |
| 126.5                    | 0                        | 95.5                   | 0                      | 30           | 293864            |
| 126.5                    | 0                        | 95.5                   | 0                      | 30           | 601024            |
| 158.1                    | 0                        | 119.4                  | 0                      | 30           | 46332             |
| 158.1                    | 0                        | 119.4                  | 0                      | 30           | 65068             |
| 158.1                    | 0                        | 119.5                  | 0                      | 30           | 85273             |
| 126.5                    | 0                        | 100                    | 0                      | 45           | 193078            |
| 126.5                    | 0                        | 100                    | 0                      | 45           | 279092            |
| 126.5                    | 0                        | 100                    | 0                      | 45           | 388165            |
| 159.1                    | 0                        | 125                    | 0                      | 45           | 76955             |
| 159.1                    | 0                        | 125                    | 0                      | 45           | 34168             |
| 159.1                    | 0                        | 125                    | 0                      | 45           | 70448             |
| 126.5                    | 0                        | 105.2                  | 0                      | 60           | 323847            |
| 126.5                    | 0                        | 105.2                  | 0                      | 60           | 163901            |
| 126.5                    | 0                        | 105.2                  | 0                      | 60           | 233280            |
| 158.1                    | 0                        | 131.5                  | 0                      | 60           | 31588             |

|       |   |       |   |    |        |
|-------|---|-------|---|----|--------|
| 158.1 | 0 | 131.5 | 0 | 60 | 31534  |
| 158.1 | 0 | 131.5 | 0 | 60 | 29602  |
| 200   | 0 | 100   | 0 | 90 | 57169  |
| 200   | 0 | 100   | 0 | 90 | 23567  |
| 200   | 0 | 100   | 0 | 90 | 40055  |
| 250   | 0 | 125   | 0 | 90 | 7462   |
| 250   | 0 | 125   | 0 | 90 | 8613   |
| 250   | 0 | 125   | 0 | 90 | 4918   |
| 200   | 0 | 115.5 | 0 | 90 | 12865  |
| 200   | 0 | 115.5 | 0 | 90 | 15897  |
| 200   | 0 | 115.5 | 0 | 90 | 14287  |
| 250   | 0 | 144.3 | 0 | 90 | 4094   |
| 250   | 0 | 144.3 | 0 | 90 | 6058   |
| 250   | 0 | 144.3 | 0 | 90 | 4014   |
| 126.5 | 0 | 111.3 | 0 | 90 | 25574  |
| 126.5 | 0 | 111.3 | 0 | 90 | 65847  |
| 126.5 | 0 | 111.3 | 0 | 90 | 178127 |
| 158.1 | 0 | 139.1 | 0 | 90 | 16684  |
| 158.1 | 0 | 139.1 | 0 | 90 | 11570  |
| 158.1 | 0 | 139.1 | 0 | 90 | 19140  |



(a)



(b)

Figure 4.15 LY12CZ life prediction under uniaxial tension/compression and pure torsion loads (a) and tension-torsion loads (b) (Yang et al., 2022).



## 5 Conclusion and Recommendation

### 5.1 Conclusion

A literature evaluation on multiaxial fatigue was conducted in this dissertation. Based on the results of this study, the following conclusions can be drawn:

- S355 steel was subjected to axial and proportional (axial and torsional) fatigue testing under stress ratios of 0 and 1 for the high-cycle area. The gathered experimental data was analysed and investigated in order to evaluate five distinct multiaxial fatigue models, which were also described and debated. It was determined that the McDiarmid's model should not be used to analyse the fatigue behaviour of S355 steel, but the models suggested by Findley and Sines are suitable alternatives.
- Crack behaviour may be anticipated by incorporating the ratio of tensile yield strength to torsional yield strength. The results of the predictions suggest that the proposed model is applicable to all materials. The accuracy of the suggested model for different materials must be confirmed.
- The titanium alloy TC4 exhibits increased hardening at 45° and 90° out-of-phase loading conditions. Nonproportional loading routes have a negligible influence on fatigue damage in regions with a short life.
- For ductile materials, multiaxial models accurately predict the direction of the fatigue crack plane for 42CrMo4 steel but less accurately for AISI 303 stainless steel owing to its increased extra cyclic hardening impact. This finding seems to show that the use of multiaxial fatigue models is dependent on the material type and microstructure features.

Multiaxial stress experiments are much more complicated and costly than uniaxial fatigue experiments. Most studies use the varied phase angle as a non-proportional characteristic parameter to manage the multiaxial fatigue test procedure in the restricted multiaxial fatigue experiment. However, from an engineering standpoint, it is difficult to explain multiaxial random loading using the phase difference parameter. On the other hand, the frequency domain characteristics of the random load are readily accessible. There is a dearth of literature on non-proportional multiaxial fatigue studies with varying frequency ratios (Brown & Miller, 1982).

Unfortunately, neither the damage produced by a multiaxial fatigue stress state nor the method for assessing it are well recognized. Consequently, it is a fully unexplored subject

that continues to be investigated. Existing multiaxial non-proportional fatigue methods are restricted to the theoretical research phase, with limited practical applications. The fundamental reason is that the engineering load is complicated and unpredictable. As mentioned, multiaxial fatigue is a complicated phenomenon; thus, it should not be transformed into an equal condition of uniaxial stress using a simple static premise.

## **5.2 Further Work Recommendation**

It is proposed that the next project be focused on laboratory experiments due to the prevalence of Steel S355 throughout all of Norway and its relevance in all facilities and constructions. Title options can be "Fatigue life prediction of S355 steel under biaxial variable amplitude loading".

## 6 Reference

- ASTM, E. (2013). Standard terminology relating to fatigue and fracture testing. In: February.
- Brown, M., & Miller, K. (1982). Low-cycle Fatigue and Life Prediction, ASTM STP 770, American Society for Testing and Material. In: Philadelphia.
- Carpinteri, A., Spagnoli, A., & Vantadori, S. (2011). Multiaxial fatigue assessment using a simplified critical plane-based criterion. *International Journal of Fatigue*, 33(8), 969-976.
- Dang-Van, K. (1993). Macro-micro approach in high-cycle multiaxial fatigue. *ASTM special technical publication*, 1191, 120-120.
- Dantas, R. G. R. (2019). Fatigue life estimation of steel half-pipes bolted connections for onshore wind towers applications.
- Fatemi, A., & Shamsaei, N. (2010). Multiaxial fatigue modeling and some simple approximations. International Conference on Multiaxial Fatigue and Fracture,
- Findley, W. N. (1959). A theory for the effect of mean stress on fatigue of metals under combined torsion and axial load or bending. *Journal of Engineering for Industry*, 81(4), 301-305.
- Hudok, D. (1990). Properties and selection: irons, steels, and high-performance alloys. *Metals handbook*, 1, 200-211.
- Jahed, H., Varvani-Farahani, A., Noban, M., & Khalaji, I. (2007). An energy-based fatigue life assessment model for various metallic materials under proportional and non-proportional loading conditions. *International Journal of Fatigue*, 29(4), 647-655.
- Kallmeyer, A. R., Krgo, A., & Kurath, P. (2002). Evaluation of multiaxial fatigue life prediction methodologies for Ti-6Al-4V. *J. Eng. Mater. Technol.*, 124(2), 229-237.
- Kamal, M., & Rahman, M. (2018). Advances in fatigue life modeling: A review. *Renewable and Sustainable Energy Reviews*, 82, 940-949.
- Kim, K., Nam, K., Kwak, G., & Hwang, S. (2004). A fatigue life model for 5% chrome work roll steel under multiaxial loading. *International Journal of Fatigue*, 26(7), 683-689.
- Kristina, O. (2007). Material Data Derivation for the Fatemi and Socie Critical Plane Model. In.
- Lee, Y.-L., Barkey, M. E., & Kang, H.-T. (2011). *Metal fatigue analysis handbook: practical problem-solving techniques for computer-aided engineering*. Elsevier.

- Liu, K. (1993). A method based on virtual strain-energy parameters for multiaxial fatigue life prediction. *ASTM special technical publication, 1191*, 67-67.
- Maktouf, W., Ammar, K., Naceur, I. B., & Saï, K. (2016). Multiaxial high-cycle fatigue criteria and life prediction: Application to gas turbine blade. *International Journal of Fatigue, 92*, 25-35.
- Margetin, M., Durka, R., & Chmelko, V. (2016). Multiaxial fatigue criterion based on parameters from torsion and axial SN curve. *Frattura ed Integrita Strutturale(37)*, 146-152.
- McDowell, D. L., & Ellis, R. (1993). *Advances in multiaxial fatigue* (Vol. 1191). ASTM International.
- Miller, K. J., Brown, M. W., & Brown, M. (1985). *Multiaxial Fatigue: A Symposium*. ASTM International.
- Milne, I. (1994). The importance of the management of structural integrity. *Engineering Failure Analysis, 1(3)*, 171-181.
- Milne, I., Karihaloo, B., & Ritchie, R. (2003). 1.01-Structural Integrity Assurance. In *Comprehensive structural integrity* (pp. 1-24). Elsevier Ltd.
- Ohkawa, I., Takahashi, H., Moriwaki, M., & Misumi, M. (1997). A study on fatigue crack growth under out-of-phase combined loadings. *Fatigue & Fracture of Engineering Materials & Structures, 20(6)*, 929-940.
- Reis, L., Li, B., & De Freitas, M. (2006). Analytical and experimental studies on fatigue crack path under complex multi-axial loading. *Fatigue & Fracture of Engineering Materials & Structures, 29(4)*, 281-289.
- Sæstad, A. (2015). *Comparative study of deterministic and probabilistic fatigue assessment methods* [University of Stavanger, Norway].
- Schijve, J. (2003). Fatigue of structures and materials in the 20th century and the state of the art. *International Journal of Fatigue, 25(8)*, 679-702.
- Schütz, W. (1996). A history of fatigue. *Engineering fracture mechanics, 54(2)*, 263-300.
- Shetty, M. (2013). *Dislocations and mechanical behaviour of materials*. PHI Learning Pvt. Ltd.
- Sines, G. (1955). *Failure of materials under combined repeated stresses with superimposed static stresses*.
- Socie, D. (1993). Critical plane approaches for multiaxial fatigue damage assessment. *ASTM special technical publication, 1191*, 7-7.

- Socie, D., & Marquis, G. B. (2000). *Multiaxial fatigue*. Society of Automotive Engineers Warrendale, PA.
- Van Lieshout, P., Den Besten, J., & Kaminski, M. (2017). Validation of the corrected Dang Van multiaxial fatigue criterion applied to turret bearings of FPSO offloading buoys. *Ships and Offshore Structures*, 12(4), 521-529.
- Wang, L., Li, W. Z., & Sui, T. Z. (2010). Review of multiaxial fatigue life prediction technology under complex loading. *Advanced Materials Research*,
- Wu, Z.-R., Hu, X.-T., & Song, Y.-D. (2014). Multiaxial fatigue life prediction for titanium alloy TC4 under proportional and nonproportional loading. *International Journal of Fatigue*, 59, 170-175.
- Yang, J., Gong, Y., Jiang, L., Lin, W., & Liu, H. (2022). A multi-axial and high-cycle fatigue life prediction model based on critical plane criterion. *Journal of Materials Research and Technology*.